ESSA RESEARCH LABORATORIES
Air Resources Laboratories
Silver Spring, Maryland
May 1968

Atmospheric Transport and Diffusion in the Planetary Boundary Layer

Technical Memorandum ERLTM-ARL 5

U.S. DEPARTMENT OF COMMERCE / ENVIRONMENTAL SCIENCE SERVICES ADMINISTRATION

ESSA RESEARCH LABORATORIES

AIR RESOURCES LABORATORIES

IMPORTANT NOTICE

Technical Memoranda are used to insure prompt dissemination of special studies which, though of interest to the scientific community, may not be ready for formal publication. Since these papers may later be published in a modified form to include more recent information or research results, abstracting, citing, or reproducing this paper in the open literature is not encouraged. Contact the author for additional information on the subject matter discussed in this Memorandum.

U.S. DEPARTMENT OF COMMERCE
ENVIRONMENTAL SCIENCE SERVICES ADMINISTRATION
RESEARCH LABORATORIES

ESSA Research Laboratories Technical Memorandum -ARL 5

ATMOSPHERIC TRANSPORT AND DIFFUSION IN THE PLANETARY BOUNDARY LAYER

I. Van der Hoven, Editor

Contributors

J. K. Angell
D. L. Bjorem
C. R. Dickson
G. A. Herbert
D. H. Slade
G. E. Start
L. L. Wendell

Air Resources Environmental Laboratory
Silver Spring, Maryland 20910

Semiannual Research Program Review
July - December 1967
for the Division of Reactor Development and Technology
U. S. Atomic Energy Commission

AIR RESOURCES LABORATORIES
TECHNICAL MEMORANDUM NO. 5

SILVER SPRING, MARYLAND 20910
MAY 1968

Preface

In accordance with the letter of agreement of July 10, 1967, with the U. S. Atomic Energy Commission, Division of Reactor Development and Technology, Environmental and Sanitary Engineering Branch, the Air Resources Laboratories have continued their study of atmospheric transport and diffusion in the planetary boundary layer, micrometeorology, diffusion climatology, and the application of this work to the disposal of radioactive waste gases into the atmosphere. The research is technically administered and supervised through the Air Resources Environmental Laboratory of the Air Resources Laboratories. The work is performed at the Air Resources Laboratories Headquarters in Silver Spring, Maryland, and at the Air Resources Idaho Falls Laboratory, National Reactor Testing Station, Idaho. Any inquiry on the research being performed should be directed to the editor, Isaac Van der Hoven, Chief, Air Resources Environmental Laboratory, Air Resources Laboratories, Environmental Science Services Administration, 8060 13th Street, Silver Spring, Maryland 20910.

Table of Contents

ATMOSPHERIC TRANSPORT AND DIFFUSION

IN THE PLANETARY BOUNDARY LAYER

AIR RESOURCES LABORATORIES SEMIANNUAL RESEARCH PROGRAM REVIEW
FOR THE ENVIRONMENTAL AND SANITARY ENGINEERING BRANCH
DIVISION OF REACTOR DEVELOPMENT AND TECHNOLOGY
U. S. ATOMIC ENERGY COMMISSION

JULY - DECEMBER 1967

1.0 RESEARCH AT AIR RESOURCES LABORATORIES HEADQUARTERS, SILVER SPRING, MD.

1.1 Low Altitude Constant Volume Balloon (Tetroon) Trajectories

(This program is a joint effort by personnel of the Air Resources Laboratories in Silver Spring, Maryland, and field offices. Support is provided jointly by the Atomic Energy Commission and the Public Health Service.)

Since there is good reason to assume that the motion of a freely floating constant volume balloon (tetroon) follows the motion of an air parcel, the technique of the radar positioning of these tetroons has proven useful in determining air trajectories and in computing the Lagrangian statistics of turbulence that form the basis for current atmospheric turbulence and diffusion theory. In addition, the technique provides an opportunity to compare Lagrangian (moving coordinates) and Eulerian (fixed coordinates) measurements.

A paper entitled "Eddy Velocities in the Planetary Boundary Layer Obtained from Tetroon Flights at Idaho Falls" is undergoing internal review. This paper considers tetroon-derived eddy velocity, stress, and mechanical energy generation as functions of height (up to 2 km), lapse rate, and wind speed. At the National Reactor Testing Station (NRTS) the rms vertical velocity increases strongly with respect to these parameters, whereas the lateral velocity increases appreciably only with wind speed. Of considerable interest is the partitioning of the rate of production of eddy kinetic energy by the shear of the mean flow. Under relatively unstable conditions this mechanical energy generation is associated mainly with vertical shear of the lateral mean wind rather than the longitudinal mean wind. The average value of the stress under relatively unstable conditions (nearly 6 dynes cm^{-2}) indicates that large amounts of momentum are abstracted from the mean flow in this region.

Analysis is proceeding on overwater tetroon flights from Wallops Island, Virginia, and at Bodega Bay, California. Special emphasis will be placed on the change in flight parameters as the tetroon moves from sea to land.

Programming difficulties have slowed the analysis of tetroon vertical periodicities as a function of lapse rate. This analysis, aimed at assessing the validity of the Brunt-Vaisala formulation in the atmosphere, will be carried out as soon as these difficulties are overcome.

1.2 Vertical Variation of Lateral Turbulence

According to the literature, the standard deviation of the lateral wind component, σ_v, is thought to be invariant with height, at least in the first hundred meters above the surface. An investigation of the data from about one dozen sites (table 1) does not appear to confirm this supposition. Rather, σ_v appears to increase with increasing height through some surface-based interval, then to reach a maximum value, and finally to begin a regular decrease above the maximum.

To model this situation, it was decided to work through the commonly used identity

$$\sigma_v = \sigma_\theta \bar{u}, \tag{1}$$

where σ_θ is the standard deviation of the horizontal wind direction distribution and $\bar{u}$ is the speed of the mean wind vector. Assuming logarithmic functions to describe the vertical variation of σ_θ and $\bar{u}$, one could show that, for neutral conditions, the height of the maximum value of σ_v (z_{max}) is given by

$$z_{max} = z_o \; e^{a/2b}, \tag{2}$$

where z_o is the roughness length and a and b are constants obtained from the observed σ_θ profile. This model gives a fair fit to observed values of z_{max}.

The investigation of the vertical profiles of σ_θ showed that (1) a function of the form $\sigma_\theta = a - b \ln \frac{z}{z_o}$ fits most of the profiles for any stability, (2) the σ_θ profiles are better stratified with respect to stability when plotted against $\ln z/z_o$ rather than z alone, and (3) there appears to be a tendency for σ_v to increase from the surface to some level and to decrease above that level.

Also, use of the wind direction range seems to furnish values of σ_θ that are grossly compatible with those obtained by more precise techniques.

The results of this work are being assembled and will shortly be submitted for review and publication.

Table 1. Summary of Data Used

Location	Original data form	Sampling heights used (m)	Stability	Number of profiles	Sampling time (min)	z_o (m)
Damascus, Md.	R, $\bar{u}$	4, 15, 30, 61	Near Neutral	9	60	0.10
Dugway Proving Grounds, Utah	σ_θ, $\bar{u}$	σ_θ- 2, 5, 15 $\bar{u}$- 0.7, 2, 4, 8, 16	Unstable Stable	16	10	0.015
Hanford Richland, Wash.	σ_θ, $\bar{u}$	0.8, 1.5, 3, 6, 12, 24	Near Neutral	9	20	0.03
National Severe Storms Lab. Norman, Okla.	R, $\bar{u}$	445 m	Unstable	60 (data at 435 m only) July and August	60	-
O'Neill, Nebr.	i_v, σ_v, $\bar{u}$	1.5, 3, 6, 12	Stable Near Neutral Unstable	40	10	0.01
Philadelphia, Pa.	R, $\bar{u}$	30, 61, 107, 175, 270	Very Stable Stable Unstable	70	60	2.9
Round Hill, Mass.	σ_θ, $\bar{u}$	σ_θ- 16, 40 $\bar{u}$- 1, 2, 4, 8, 16, 32, 40.	Stable	3	60	0.10
(Project Sandstorm) Edwards AFB, California	σ_θ, $\bar{u}$	4, 15, (σ_θ) 30, 61	Unstable	19	8.5	-
White Sands, New Mexico	σ_θ, $\bar{u}$	4, 19, 33, 62	Stable Unstable	15	60	0.10
White Sands, New Mexico	σ_θ	5, 12, 27, 41, 62	Stable Neutral Unstable	-	10	0.10
(Project Windy Acres) Liberal, Kansas	σ_θ, $\bar{u}$	σ_θ- 2, 32 $\bar{u}$- 0.25, 0.50, 1.0, 2, 4, 8, 16, 32	Stable Near Neutral	23	15	0.01

1.3 Wind Persistence Probability

An increasing amount of interest is being expressed in quantitative analyses of the time persistence of wind direction. For example, in connection with the emission of an effluent into the atmosphere over a period ranging from hours to days, it is desirable to have probability statistics on the time persistence of wind in a given sector in order to compute the average downwind concentration of the effluent.

A wind direction persistence evaluation using 5 years of standard hourly reports from each of 61 weather stations in the United States has been completed, and a technical report is being prepared. In essence the study involves the computer determination of the probability that a wind direction would persist in various sectors of given size for hourly periods, starting with 2 hr, and as a function of the direction of the center of the sector, the season, and the wind speed for each of the stations.

There is strong evidence that wind direction persistence is related to wind direction frequency. Indeed, it is reasonable to expect that the more frequently a wind blows from a sector, the longer will be the periods in which the wind continuously persists in that direction. This is graphically shown in figure 1, where for Galveston, Texas, the percent probability of a wind direction persisting for a 5-hr period in a 22 1/2° sector is plotted against the percent frequency in that direction. A line of least squares fit is drawn through the winter data (closed circles) and the summer data (open circles) with a correlation coefficient of 0.95 each. Also noted is the greater persistence of wind direction in winter than summer. In general, these relationships were valid regardless of geographical location.

The effect of geographical location upon wind direction persistence is shown in figure 2 where the maximum number of hours (regardless of season) on the basis of a 10 percent wind persistence probability in a 22 1/2° sector centered on the indicated 16-point compass direction is plotted for the 61 stations in the United States. Thus for example, the highest maximum value at the 10 percent level was 10.0 hr for Corpus Christi, Texas, for winds from the southeast, and the lowest maximum value was 3.5 hr for Phoenix, Arizona, for winds from the east. It is difficult to see any well-defined geographical patterns in figure 2 except for a tendency for the lower values of wind direction persistence to occur in the mountainous regions of the Rockies and the Appalachians. The region of most persistent wind direction seems to be the Texas Gulf Coast and, to a lesser degree, the tier of states to the north.

The wind direction persistence was also categorized according to wind speed classes. As one would expect, the higher the wind speed the greater the tendency for the wind to remain in a given sector. Figure 3 shows a plot of such an analysis for Daytona Beach, Florida, for a 22 1/2° sector width. For example, at the 10 percent probability level the wind will persist in a 22 1/2° sector for about 3.5 hr in the speed range of 1 - 5 mph and increases consistently to a value of about 7.0 hr in the 16 - 20 mph range.

1.4 Boundary Layer Turbulence

An interim report on the primary results of the New Jersey marsh study was prepared and submitted to the project supervisor, Professor A. K. Blackadar of the Pennsylvania State University. This study was conducted at a controlled roughness discontinuity on a salt-water marsh at Sayre's Neck, New Jersey (Blackadar et al., 1967), and most of the results were summarized in the previous semiannual report. Recently a detailed amplitude-statistic analysis was conducted to define the distribution of vertical velocity fluctuations and the first four statistical moments. The overall appearance of the probability density function is very similar to that of the standard normal. In most cases the skewness was a small negative value, ranging from -0.1 to -0.27, and the large percentage of the kurtosis values was positive, ranging from 3.0, the value for the standard normal, to 4.5. A more detailed study of the kurtosis for the high frequency fluctuations in the region of the internal boundary layer is being conducted at this time.

A reevaluation of all computer programs using the CDC-6600 at Suitland, Maryland, has been made necessary by a change in the program processor. Minor changes were necessary in all programs. At the same time we have changed from the lag-correlation method of computing the power spectra to the faster Cooley-Tukey algorithm. Data tapers and field splitting techniques suggested by Cooley et al. (1967) are being tested on the new "scope" operating system.

2.0 RESEARCH AT NATIONAL REACTOR TESTING STATION, IDAHO

2.1 Radar-Tetroon-Transponder System

The development of the radar-tetroon-transponder system, to attempt to trace atmospheric motions, has heightened interest in computing various parameters of turbulence and diffusion from observed Lagrangian data. During the interpretation of computational results based on such data, the investigator should be concerned with two questions: First, how well does the motion of the tetroon approximate the motion of the atmosphere? Second, and not necessarily second in importance, how accurate is the tracking information obtained by the radar? Clearly, if the second question cannot be answered satisfactorily, one need not ask the first.

Causes of tracking error may be placed into two general categories: 1) external causes inherent in electromagnetic wave propagation and 2) internal causes related to the electronic and mechanical systems of the radar itself. The external causes, dependent primarily on atmospheric conditions, are beyond the control of our investigations. This is not to say they should be ignored. The internal causes, dependent primarily on the quality of the equipment, are in a realm where the investigators have some control. Practicality asks: just how good the equipment has to be to give sufficiently accurate tracking information? The answer to this, of course, depends on the use intended for the tracking information. The term

"sufficiently accurate" is a relative consideration. If the information is to be used to determine relative velocities between two or more targets, a high level of accuracy is mandatory.

One of the purposes of this analysis is to investigate the effects of varying degrees of tracking errors, due to internal causes, on the tetroon time series of position and velocity. This is to be done by direct observation as well as comparison of such quantities as the autocorrelation fuctions and energy spectra. Another purpose of the study is the evaluation of the effectiveness of smoothing in removing the effect of these errors. It is hoped that a future field test of two radars tracking the same balloon under different atmospheric conditions will help to evaluate the various types of errors.

The following study is based on a simple consideration of the errors due to internal causes. The fact that the radar manufacturers publish rms error figures for range, azimuth, and elevation suggests the possibility of a normal distribution of these errors. This would mean that at any given instant in time the radar could report the position of the object being tracked as being located in a three-dimensional envelope about the true location of the particle. The size of the envelope would vary with the tracking accuracy of the radar and the distance of the target from the radar. Because the error is assumed to be of a random nature, the variation of a particle position within the envelope from one reading to the next can have a very marked effect on the velocities computed from the recorded positions.

To estimate the effect of these random errors, data from a previously tracked flight may be assumed to be the data for a trajectory in which the positions have somehow been exactly determined. To simulate trajectories that might be obtained from a radar with a random tracking error, one need only to superimpose these random errors onto the time series of range, azimuth, and elevation readings of the "exact" trajectory and recompute the positions and velocities.

The above procedure was carried out as follows: Assume that for the "true" trajectory θ, φ, and R represent azimuth, elevation, and slant range, respectively, and that $\Delta\theta$, $\Delta\varphi$, and ΔR represent the rms error values published by the manufacturer of a given radar. The simulated trajectory positions are given by:

$$x_i = (R_i + r_i \Delta R) \text{ Cos } (\varphi + s_i \Delta\varphi) \text{ Cos } \left[(450^\circ - \theta_i) + t_i \Delta\theta\right] \qquad (3)$$

$$y_o = (R_i + r_i \Delta R) \text{ Cos } (\varphi + s_i \Delta\varphi) \text{ Sin } \left[(450^\circ - \theta_i) + t_i \Delta\theta\right] \qquad (4)$$

$$z_i = (R_i + r_i \Delta R) \text{ Sin } (\varphi + s_i \Delta\varphi), \qquad (5)$$

where x, y, and z are aligned with y toward the north, x toward the east, and z toward the zenith direction. In (3), (4), and (5) r_i, s_i, and t_i represent numbers between -1 and +1 selected randomly from a normal distribution. The subscript i varies from 1 to the number of discreet positions in the "exact" trajectory. For the purposes of this study the curvature of the earth effect on z_i was neglected.

The mean velocities under consideration are then represented by:

$$u_i = (x_{i+1} - x_i)/\Delta t \tag{6}$$

$$v_i = (y_{i+1} - y_i)/\Delta t \tag{7}$$

$$w_i = (z_{i+1} = z_i)/\Delta t \ . \tag{8}$$

To study the effects of error on the velocities, it was not considered necessary to rotate coordinates to make u represent the along-stream component of velocity and v the cross-stream component.

The smoothing done on parameter Q of the data containing the random errors was a simple running average represented by

$$\overline{Q}_i = \frac{1}{N} \left[Q_{(i-\frac{N-1}{2})} + Q_{(i-\frac{N-1}{2}+1)} + \ldots Q_{(i)} + \ldots . Q_{(i+\frac{N-1}{2})} \right] , \tag{9}$$

where N is the number of points used in the running average.

Two trajectories were selected to represent the "actual" data. One was tetroon flight 7, released from Wallop's Island, Virginia, and tracked with an FPS16 radar. The flight of this tetroon was practically straight and level, indicating very stable conditions. The other trajectory chosen was tetroon flight 36, released at the NRTS. The vertical oscillations in this flight indicated unstable atmospheric conditions. Flight 36 was tracked beyond a range of 40 miles while flight 7 was tracked slightly more than 20 miles.

The values for ΔR, $\Delta\theta$, and $\Delta\varphi$ used were the rms values given for three different tracking radars, the M33, the WF3, and the FPS16. The rms error values used are shown in table 2.

Table 2. Root-mean-square values of range, azimuth, and elevation bearing errors.

	ΔR	$\Delta\theta$	$\Delta\varphi$
WF3	100 yds.	$.25^{o}$	$.25^{o}$
M33	5 yds.	$.075^{o}$	$.075^{o}$
FPS16	5 yds.	$.01^{o}$	$.01^{o}$

The hypothetical position of the particle would have a .318 probability of being inside an envelope around the "true" position bounded by $(R\pm\Delta R)$, $(\theta\pm\Delta\theta)$, and $(\varphi\pm\Delta\varphi)$, and a .870 probability of being in an envelope bounded by $(R\pm 2\Delta R)$, $(\theta\pm 2\Delta\theta)$, and $(\varphi\pm 2\Delta\varphi)$. Computations are carried out for both position limits using the three specified ranges of errors given in table 2.

The quantities computed are the time series of height, horizontal velocity, vertical velocity, and the mean, variances, and autocorrelation functions for u, v, and w. Calculations were made with 2 rms envelopes for no smoothing and three-point smoothing, for the three radars, and for the NRTS and Wallop's Island flights. Calculations for 1 rms envelopes were made using no smoothing, three-point smoothing, and seven-point smoothing, for both tetroon flights, and for the WF3 and M33 radars. The 2 rms errors for the FPS16 were so small that 1 rms errors were not calculated. The vertical heights are given in meters and the horizontal and vertical speeds are in meters per second. Sample diagrams of velocity traces for the horizontal and vertical components have been included in figures 4 - 8 for the M33 specifications, because 1) it is the radar which has been used extensively for tracking tetroons and gathering turbulence data, and 2) because its error specifications lie between those of the WF3 and the FPS16. Only plots involving the NRTS flight are included for illustration.

In figure 4 a time series plot of the horizontal velocity for the original trajectory data of flight 36 is shown on the upper graph. On the lower graph the horizontal velocity trace is shown for the original data plus random errors bounded by $\pm$ 1 rms values . The change due to the error is slight. In figure 5 the same quantities are plotted for error bounds of $\pm$ 2 rms values. The third graph contains the time series of the same original data plus a second set of random errors, simply for comparison with the first set including random errors. The larger errors in the 2 rms set of data have caused a significant amount of error, especially in the higher frequency oscillations, and, as one would expect, the effect of the errors increases as the target is farther from the radar. In figure 6, the three velocity traces shown are the smoothed versions of the traces shown in figure 5. The running average or smoothing interval used (9) was three points, which is equivalent to a mean over 3 min of tracking time. The notable feature in this illustration is the close resemblance of all three traces. Some of the high frequency oscillations have been removed. More significant is that most of the effect of random error seems to have been removed. The close

resemblance of the bottom two traces bears this out, because they contained two different sets of random error. Figures 7 and 8 illustrate the vertical component of velocity in the format of figures 5 and 6, and conclusions similar to those for horizontal velocities may be drawn here. The principal differences are that random errors affect the vertical component of velocity more seriously than the horizontal component and that the smoothing does not appear to be as effective in removing the random error as in the case of the horizontal velocity traces.

To further visualize the effect of random position errors and data smoothing, autocorrelation functions for the u, v, and w velocity components are presented for the WF3 radar. The solid curve represents the autocorrelation of the original data, the dashed curve the autocorrelation of the original data plus the random error. The autocorrelations for no smoothing, and for three- and seven-point smoothing are shown in figures 9a, b, and c. The curves in these figures emphasize the effectiveness of the smoothing. The correlation curves for the original data become much more regular as the smoothing interval increases, indicating the removal of the higher frequencies. The tendency of the correlation curves for the "original data plus the random error" data to converge to the correlation curves for the original data, as the smoothing interval increases, indicates that successively greater amounts of random error are being removed. The results further indicate that the vertical component of velocity is most seriously affected by the errors.

Considering all the data, the time series plots of position and speed, the autocorrelations, and the ratios of erroneous data to "true" data, the following observations are made.

1. The effect of randomly incorporating target-bearing errors as great as $\pm$ 2 rms into range, azimuth, and elevation readings for a tetroon vary from disastrous for turbulence analysis, when values of $\pm$ rms ΔR = 100 yards, rms $\Delta\theta$ = .25° and rms $\Delta\varphi$ = .25° are incorporated, to hardly noticeable when values of rms ΔR = 5 yards, $\Delta\theta$ = .01°, and rms $\Delta\varphi \doteq$ .01° are used.

2. Smoothing, by means of a running average, reduced the effects of the random error. The plots indicate that the smoothed heights and velocities tend to converge to the smoothed "true" heights and velocities as the smoothing interval is increased. The results of this study show that for errors of the order of 2 rms, reasonable agreement is obtained between smoothed velocity traces for the following sizes of averaging interval.

Radar	Points in Smoothing Interval
WF3	7
M33	3
FPS16	0

The disadvantage of smoothing over longer periods is the removal of actual high frequency information with the smoothing out of random errors.

3. The autocorrelation plots yield the following preliminary guides for smoothing:

Points in Smoothing Interval

	u	v	w
WF3	5 to 7	5 to 7	7
M33	3	3 to 5	3 to 5
FPS16	< 3	≤ 3	3 to 5

The impact of this smoothing on the measurement of higher frequency atmospheric turbulence (periods of turbulent fluctuations less than twice as long as the smoothing interval) becomes important. These smoothing figures are based on random 2 rms error envelopes. With a 1 rms error envelope the smoothing interval could be shortened. It appears caution is necessary when considering tetroon motion features which approach or are shorter than the 2 rms smoothing period.

In approaching the problem of tracking accuracy in the previous section, our basic assumption is that the errors in range, azimuth, and elevation data occur randomly. This assumption causes the errors in the velocities to be much more severe than if the range, azimuth, and elevation data were somehow systematically in error.

Probably one of the most direct methods to gain information on the true nature of positioning error in a radar is to simultaneously track the same target with two or more radars and compare the results. Data of this type were recently obtained from two radars in England, where a Plessey WF3 and a WF44S were used to simultaneously track 30 separate pilot balloons. The WF44S radar was used as the standard, since it was assumed to be more accurate than the WF3. The accuracy was quoted at $.07^{o}$ for both elevation and azimuth and 40 m rms for range. This radar's range accuracies are less than the M33 radar which we use. Data were obtained only after both radars had locked on the balloon and then collected until one radar lost it. The data recordings were synchronized to the nearest second.

The tracking data obtained from two radars which have simultaneously followed the same target can be regarded as data from two targets flying concurrently. The difference in the position and motion of the "two" targets is then the result of the relative tracking error between the two radars. Since one of the radars (WF3) used in the test was being evaluated

for the purpose of determining upper level winds, the analysis was carried out on balloon horizontal direction, horizontal and vertical velocity, and height.

A visual comparison was made of time series plots of height, wind direction, and velocity based on the data from one radar and, on the same graphs, the time series plots of the difference in the time series of these quantities from both radars. The means and standard deviation of the quantities were also computed for the differences.

Thirty pilot balloon flights and one tetroon flight were used for the analysis. Some typical plots of the results are shown in figures 10 through 13. The top diagram in each figure is the wind direction plotted against time, the middle diagram shows horizontal wind velocity plotted against time, and the bottom diagram is height in meters plotted against time. The absolute value plotted is the WF44S, which was used as a standard, and the variation around zero on each diagram is the variation of the simultaneous data of the WF3 radar.

An interesting observation one can make from these results is that the combined effects of the tracking error from the two radars is quite random in nature. This would indicate that the tracking error from each radar is of a random nature, which, in a way, is encouraging because the effect of a random error can be markedly reduced by smoothing techniques as was shown in the analysis of hypothetical error. However, since the smoothing also eliminates the actual higher frequencies in the target's motion, the higher (greater) the accuracy of the radar the more useful it is in measuring the turbulent motions of a target.

The increasing error of the balloon height with time, shown in figures 10 through 13, can be attributed to the difference in the leveling of the two radars, since they were not precisely leveled prior to tracking. The error seldom exceeded a few hundred meters in 10,000 m, and probably could easily be corrected.

If this comparison seems a little harsh on the radars involved, it is probably due to some ambiguity in the comparison. The diagrams were set up for examination of quantities used in reporting upper level winds, but the winds were computed from data with a sampling interval in time which was 1/10 (12 s) to 1/4 (30 s) of what it is in standard pilot balloon runs. Smoothing of the results indicated significant improvement in the deviations, but determining the character of the error in the raw data was of primary interest. For this reason, the original sampling intervals were used in computing the velocities.

We hope that an expanded analysis on simultaneous tracking data from the M33 radars will provide information on how accurately they report the motion of targets. This information will be vital in determining the extent to which tetroon data may be used in evaluating relative dispersion statistics. Radar and double theodolite simultaneous tracking experiments also are being carried out at the Air Resources Laboratory - Las Vegas, and it is hoped that these data will be useful in the radar accuracy analysis.

During the summer of 1966 an intensive tetroon experiment was carried out at the NRTS. Inasmuch as the tetroons also respond to vertical air motions, they yield estimates of three-dimensional velocity components within the planetary boundary layer. Since the values of longitudinal (along-stream), lateral (cross-stream), and vertical velocity are little known above tower height (a few hundred meters at most), it is worthwhile to analyse the numerous tetroon data from this point of view.

The results were found to provide a useful "first guess" concerning conditions and trends in the middle and upper portions of the planetary boundary layer, to be generalized later by more conventional techniques.

Tetroon positions were derived at 1-min intervals and a running mean of 3 min was used because the previous study had indicated a 3-min average is necessary to reasonably remove the high frequency random tracking errors of the M33. Position changes with time yield longitudinal (u), lateral (v), and vertical (w) velocities, which serve as the basis for the subsequent analysis, and for which rms values were computed for each flight and applied to the mean flight altitude.

Temperature soundings were obtained near the time of the tetroon flights, so that lapse rate data are available for comparison with the turbulent parameters. Unfortunately, however, the morning flights, in a relatively stable atmosphere, tended to be at a lower level than the afternoon flights in a more unstable atmosphere, so that the data are not evenly distributed in a diagram with height and lapse rate as coordinates.

Figure 14 presents the variation with height and lapse rate of each of the three rms velocities. Each of the three diagrams is based on more than 10,000 1-min average values of velocity, distributed among nearly 100 flights for which rms velocity values were calculated. These flight-mean values were heavily smoothed with respect to height, lapse rate, and wind speed to yield the smooth variations noted in figure 14 and subsequent diagrams.

The right-hand diagram of figure 14 shows that the rms vertical velocity (σ_w) at a height of 2.0 km is half again that at a height of 0.5 km, and nearly doubles as the lapse rate changes from half the dry adiabatic value to the dry adiabatic value (note that the lapse rate slightly exceeds the dry adiabatic through the vertical extent of some of the afternoon flights). The rms lateral velocity (σ_v) shows very little trend, while the rms longitudinal velocity (σ_u) shows just the opposite trend, i.e., a decrease in value with increase in height and lapse rate. The latter is due to the large variation in u that occurs in the morning (relatively stable lapse rate) in this area when the nighttime northeasterlies give way to the daytime southwesterlies; it would not show up in most nonmountainous areas.

Figure 15 shows rms velocity as a function of height and wind speed. Wind speed and lapse rate are not completely independent at the NRTS, stronger winds being associated with the afternoon instability, even at tetroon flight level. Thus it is not surprising to find that σ_w increases with wind speed, although it does so less strongly than with lapse rate;

however, σ_v increases with wind speed whereas it did not increase with lapse rate. Variations in σ_w seem to be more closely associated with lapse rate (buoyancy) changes, while the changes in σ_v and perhaps σ_u are more closely attuned to wind speed changes.

Figure 16 shows values of $\frac{\sigma_v}{\sigma_u}$ and $\frac{\sigma_w}{1/2(\sigma_u+\sigma_v)}$ as functions of height, lapse rate, and wind speed. Both ratios, particularly the latter, increase with height and lapse rate, and it is interesting that both ratios approach the value one at heights near 2 km in neutral conditions despite the probable underestimate of vertical air velocities by the tetroon. This is a reflection of the helical circulations prevalent in the region at the time. The variation of these ratios with wind speed is similar but less pronounced.

The variation of turbulence intensity with height and lapse rate during the summer is shown in figure 17. The vertical turbulence intensity $\sigma_w/\bar{U}$ decreases with height and increases with lapse rate only below a height of 1 km. The horizontal components decrease both with height and lapse rate. Again, the latter effect is associated with large meandering during the morning hours.

Figure 18 shows the variation of a $\sigma_w/\bar{U}$ with height for near-neutral conditions (solid line connecting dots) when σ_w is determined from the right-hand section of figure 17. The solid line connecting circles, depicting vertical turbulence intensity versus height, stems from a regression line of the variation of $\sigma_w/\bar{U}$ with height determined from tetroon flights throughout the year. The agreement of the two curves in the region of overlap is slightly disconcerting in that the mean lapse rate on which the regression line data is based should be somewhat less than dry adiabatic. Regardless of the magnitude comparison, however, the implication is that $\sigma_w/\bar{U}$ decreases less rapidly with height as one progresses upward through the planetary boundary layer.

At the heights depicted in figure 18, the best vertical velocity data available for comparison are those obtained by Pasquill (1967). He determined, through the use of barrage balloons at Cardington, England, the rms angular deflection in the vertical of a bivane at heights of 0.3 and 1.2 km, based on a sampling time of 1 hr and an averaging time of 1/2 min. The dashed line in figure 18, representing Pasquill's results in near-neutral stability conditions, shows that the decrease of $\sigma_w/\bar{U}$ with height at Cardington is similar to that derived from the tetroon flights at the NRTS, but that the magnitude of $\sigma_w/\bar{U}$ at Cardington is only about half that at the NRTS. This twofold difference in vertical turbulence intensity is in general agreement with 1) the order of magnitude difference in heat flux at NRTS and Cardington at the given times of year, 2) the assumption that the dissipation is proportional to vertical heat flux (neglect of both mechanical generation of turbulence and flux divergence), and 3) that, from dimensional considerations, the rms vertical velocity is proportional to the cube root of the product of dissipation and height (i.e. $\sigma_w \sim \varepsilon^{1/3} z^{1/3}$).

One can obtain the vertical flux of momentum, or horizontal Reynolds stress, from tetroon flights by evaluating covariance between vertical and longitudinal velocity along each flight, i.e., $\tau = -\rho\overline{u'w'}$ where ρ is density and u' and w' are deviations from flight-mean values of longitudinal and vertical velocity. Based on summer data alone, the top diagrams of figure 19 indicate increased stress with height and wind speed but little variation of stress with lapse rate. The increase of stress with wind speed is certainly to be expected, but the increase with height is somewhat puzzling and probably results from the mixture of relatively low-level flights in the morning (small stress) and relatively high-level flights in the afternoon (large stress), or from the advection of mechanical turbulence from the mountains to the higher levels over the valley.

The rate of production of eddy kinetic energy (K_e) due to the shear of the mean flow is given by

$$\dot{K}_e = -\overline{u'w'}\,\frac{\partial \overline{U}}{\partial z}\,, \tag{10}$$

where $\frac{\partial \overline{U}}{\partial z}$ is the vertical shear of the longitudinal wind. In this paper we have used the vertical wind shear derived from tetroon flights, even though there is evidence that the shear so obtained is an underestimate of the true shear. Consequently, the values of $\dot{K}_e$ cited are probably conservative.

The lower left diagram of figure 19 shows that $\dot{K}_e$ decreases strongly with increasing lapse rate and becomes almost zero as the lapse rate exceeds the adiabatic. Presumably, then, in relatively unstable atmospheres the eddy kinetic energy is generated chiefly through buoyancy forces. The increase of $\dot{K}_e$ with wind speed (lower right diagram of figure 19) would be expected because a strong wind at these heights implies a large shear. The decrease of $\dot{K}_e$ with height is probably associated with the weaker shears to be expected at higher levels (logarithmic wind profile).

Although preliminary in nature, above discussion shows that the tetroon-transponder system is a useful means of estimating eddy velocity components within the planetary boundary layer. As such, it should be considered an alternative to the complex and costly barrage-balloon and aircraft systems being used within this layer. Note that if these three systems could be operated simultaneously at the same site, very basic data could be obtained on the relation among Lagrangian, Eulerian-time, and Eulerian-space statistics. Such an experiment is hoped for in the near future.

2.2 Computer Program

2.2.1 Development of Data Handling and Analysis Techniques for Turbulence Studies

The diffusion and dispersion of particles or gases in the atmosphere by the turbulent motion of eddies of all scales and intensities has long been known to be much more significant than diffusion caused solely by the

motion of molecules. For this reason, a great deal of effort has gone into the study of the turbulent motion of the atmosphere in order to gain an understanding of its structure.

Studies of atmospheric turbulent motion have been generally confined to particular ranges of eddy sizes or frequency bands because of difficulties in sampling at a relatively high rate of speed for long periods of time. Investigators interested in low frequency turbulence therefore use a series of data values, each of which represents an average over a specified interval of time. Those interested in high frequency turbulence use sensitive instruments and sample the data very rapidly for a short period of time. Thus the frequency range is selected and the sampling is done to fit the requirements. A notable experiment involving a broad range of frequency, 10^{-3} cycles/hr - 1000 cycles/hr has been carried out (Van der Hoven, 1957), but until the recent advent of reliable high-speed data acquisition systems, third generation electronic computers, and revolutionary techniques in obtaining the Fourier transform of digital data, no attempts were made to verify the spectral results of the experiment.

Interest in diffusion from releases of tracers in the atmosphere for extended periods has pointed up the need for turbulence studies involving the high frequencies, which are important in the initial diffusion, through the lower frequencies, which are important in dispersing the effluent after it has spread to larger scales. Our purpose is to establish an analysis program to apply to the turbulence data from diffusion experiments consisting of effluent releases into the atmosphere for long periods. The program is to be as completely computerized as possible, even to the point of intermediate and final plotting of analysis results. It is also to be as flexible as possible, allowing the analyst as much freedom as possible in controlling the analysis as indicated by the character of the data.

2.2.2 Data Preparation and Preliminary Analysis

The data are obtained from a Hewlett-Packard model 2010J system (fig. 20), which records analog data derived from a number of sources and displays and records this information on magnetic tape in digital form.

The inputs are d-c frequencies and resistances, but the system can measure any combination of physical parameters that are convertible by transducers to these analog forms. The system uses a digital voltmeter as the digitizer. It features a floated and guarded input, permitting accurate low level measurements in the presence of severe common mode noise. Voltage ranges are from 0.0 to 1000 V full scale, polarity sensed and indicated automatically along with auto-ranging. Input impedance is 10^7 ohms on 10, 100, and 1000 V ranges. Accuracy is $\pm$ 0.005 percent full scale $\pm$ 1 digit (0 to full scale).

Model 2010J system has a sampling speed of 18 channels per second and 12 character words. The scanner is capable of 25 channels of 12 character words.

The data from the meteorological sensing equipment is recorded in digital form on standard 1/2-in. computer-compatible magnetic tape. The recorded data are edited and recorded on another magnetic tape. The editing is simply a process of testing the data for erroneous characters or other problems that might cause error in converted data. It also includes notification of missing data words on a given scan of the sensors. Equipment reliability has improved to the point that on a recent run only one duplicate data word was produced in one scan of 25,000 scans of nine sensors each.

Important in experiments involving turbulence data collection is the ability to observe a compact historical record of wind conditions that will give a general picture of the turbulent conditions throughout a given test. For this purpose strip chart records of speed and direction, at the 61-m level for the duration of a given test, are photographed and included with other recorded information pertaining to the test. The data are recorded on the strip charts at the rate of 3 in./hr. A sample is shown in figure 21. From the strip chart record one can immediately determine the time periods of greatest interest for detailed analysis. For general observation of the details of the turbulence a computer plot may be obtained of the along-stream, cross-stream, and vertical components of the eddy velocity, u', v' and w', respectively, during the selected period. Plots of this type are shown in figures 22, 23, and 24 for the three levels on the tower, 4, 16, and 61 m. The data shown in these figures were sampled every 2 s.

The most striking feature of the three figures is the difference in the character of u' from v' and w'. The u component of the wind, in the coordinate system with the x-axis along the direction of the mean flow, is measured primarily by the cup anemometer; the v and w components are particularly sensitive to movements of the bivane. The data from the anemometers used in these measurements were subjected to a 2-s filtering in the electronics, which probably accounts, at least in part, for the relatively smoother character of u'. Also, the peaks in the variance of u, i.e. σ_u^2, occurs at lower frequencies than similar measurements of w. Another feature that shows up clearly in these figures is the larger amount of high frequency turbulence at the lower levels. Also, during the period covered the average wind direction has shifted slightly as may be noted in the general trend in v'. From these observations important information may be obtained concerning smoothing and/or filtering that needs to be applied to the data.

During the development phase of this program a CDC 1604 computer is being used. The core storage allows only 2000 data points of each component to be analyzed at one time. This means that in order to look at the longer periods, the data have to be averaged. As a preliminary test, a five-point averaging was carried out on the 61-m data shown in figure 24. The result was plotted with the same time scale for comparison purposes and is shown in figure 25. We see from the figure that the averaging over 10 s has left a data trace containing primarily oscillations with periods on the order of 30 to 60 s. Longer or shorter smoothing intervals may be applied

as desired. A running average option included in the analysis program may be used either for smoothing to eliminate noise or for filtering long period oscillations.

Autocorrelation and crosscorrelation functions are essential tools in the study of turbulence. As part of the analysis program, autocorrelation and crosscorrelation computations are included as options along with their computer plots for immediate display of results as shown in figures 26 and 27. These correlation functions were computed for the 10-s smoothed values shown in figure 25 and are presented here primarily to illustrate the graphical output of the correlation program. One can see from these results, however, that the initial data plots could have been used to determine the filtering conditions to eliminate the trend in v', which appears very noticeably in the autocorrelation curve $R_v(\tau)$. The program also has an option in which the correlation values may be saved on tape for future use in computing power and cross spectra through the conventional cosine transform method.

The power spectrum probably allows the most insight into the importance of the various scales of motion. The variance of the velocity is a measure of the total turbulent energy, but the power spectrum indicates how this energy is distributed among the various scales of motion through a transformation of the data from the time domain into the frequency domain. In the analysis program an option is included for the conventional computation of the power and cross spectra through the transformation of the correlation functions. A plot routine is being developed to graphically display these results. Because of the expense of computing the correlation functions for very long time series of data, the Fast Fourier Transform (FFT) techniques (Cooley and Tukey, 1964) have to be applied. Computer programs have been obtained, and methods for the adaption of the FFT to power spectral computations are being studied, and this efficient computational scheme may even be adopted for the indirect computation of the correlation functions.

2.3 Meso-Micro Studies

To predict weather events, stability or diffusion regimes, and plume trajectories over the NRTS, a plan has been developed involving 1) statistical prediction of synoptic, mesoscale, and microscale flows, 2) study of the dynamics and statistics observed in the mesoscale wind network over the Upper Snake River Plain, and 3) development of a mesoscale prediction model for weather events and transport within the atmospheric boundary layer. During this reporting interval research efforts have centered on developing and computer-coding the statistical prediction techniques.

Statistical prediction of mesoscale to synoptic scale flows are being attempted through a modification of the Lund (1963) map-typing technique, prompted by the need for more than one parameter. The present computer code handles up to three parameters in the typing.

The prediction of weather event occurrence (a noncontinuous variable) is being handled by discriminant analysis (as opposed to regression analysis for continuous variables) by which the observed events are separated into one of several groupings.

A study using an approach developed by Rao (1952) was conducted on NRTS mesoscale data for a sample of 16 days from the autumn of 1967. Five predictors were adopted and the flows were categorized into four groupings: 1) strong SW winds ($\geq$ 15 mph), 2) light SW winds ($<$ 15 mph), 3) N to NE winds, and 4) light and variable winds. The technique predicted 13 days out of 16 correctly, or 81 percent correct. A higher verification percentage should result with optimized predictors. Further experiments await receipt of a block of dependent data.

A network of 12 off-site, in addition to the 8 on-site, wind stations over the upper Snake River Valley has been completed over an asymmetrical grid approximately 60 mi from NE to SW, and 50 mi from NW to SE. The grid stations are listed in table 3, and locations are shown in figure 28.

Table 3. Mesoscale Network of Wind Stations

On-site Stations	Off-site Stations
EBR I	Arco (1 mi S)
CFA	Big Southern (11 mi SW)
SPERT	Aberdeen (6 mi N)
EBR II	Tabor
Grid III	Blackfoot
NRF	Idaho Falls (Radio Tower KID)
TAN	Howe (1 mi E)
LOFT	Blue Dome (5 mi SE)
	Hamer
	Monteview
	St. Anthony

Initially the data will be used for case studies relating the mesoscale wind field to the synoptic scale weather patterns. Cases of special interest are:

1) Diurnal wind patterns during weak large scale wind regimes for various seasons.

2) Diurnal wind regime during moderate to strong SW wind periods.

3) Diurnal wind regime during moderate N wind periods.

4) Winter inversion wind regimes.

5) Prefrontal, front passage, and postfrontal wind fields by seasons and by intensity of the synoptic scale disturbances.

6) Sharp direction shear lines that may lie across the valley during certain synoptic scale conditions.

The second level of sophistication in the studies is to correlate the analyzed mesoscale and synoptic wind fields to one another to establish characteristic patterns. The predominant mesoscale wind field patterns may then be related to synoptic scale weather patterns by statistical means for forecast development and by physical or dynamical means for basic understanding and improvement of, and incorporation into, the statistical forecast development. The forecast wind fields may eventually be incorporated into the dosage forecasts to be used in conjunction with reactor tests.

2.4 Relative Diffusion and Deposition of Uranine Dye and Radioiodine

During November of 1967 a field test was undertaken to measure and compare the diffusion and deposition of uranine dye and elemental radioiodine.

A single field release of elemental radioiodine and uranine dye was performed on grid III during the afternoon of November 30, 1967. Effluent sampling was conducted within the 80^{o} sector shown in figure 30. There were five concentric arcs at 200, 400, 800, 1600, and 3200 m downwind of the release point (the apex of the sampling grid). Each circle on the arcs shown in figure 29 represents an air sampling position. In the actual field test, alternate sampling positions were used, beginning with the first sampler at the left side of the arc.

Air samples were collected by Staplex high volume air samplers mounted 1 m above the ground. Particulate matter was collected on glass-fiber-type filters, known commercially as Hurlburt X-934H, and backed with a dust filter. Gaseous radioiodine was collected by carbon cartridges inserted in the Staplex samplers behind the glass fiber and dust filters.

Collection efficiencies for glass fiber filters and carbon cartridges are the following: Glass fiber filters have a collection efficiency of 100 percent for 1μ particles, such as generated with uranine dye; collection efficiency for gaseous elemental iodine is from 0.1 to 0.01 percent. Carbon cartridge collection efficiency for gaseous iodine is about 95 percent. Therefore, iodine collected in the glass filter must be attached to a particulate. The assumption will be made that iodine collected on the glass filter is attached to particulate matter in the atmosphere before passage through the glass filter. (Laboratory tests will be conducted shortly to verify whether radioiodine can be captured by glass filters preloaded with uranine dye .)

The uranine dye and radioiodine effluents were released simultaneously near the apex of the diffusion grid, separated laterally about 5 ft. The tracer releases lasted for 30 min. The source strength of uranine dye was 525 g of dye; the radioiodine source was 1.19 curies. The uranine dye release rate was constant; the radioiodine release rate was somewhat irregular. The implications of a nonsteady release will be discussed with the general results of the test.

Measurements of the deposition of radioiodine on carbon fallout plates were also made. Twenty-one carbon fallout plates were positioned on the five arcs of the grid but only 4 plates were within the boundaries of the plume.

A NRTS type bivane and Beckman-Whitley cup anemometer were placed at 1, 4, 6, 16, and 61 m levels on the grid III meteorological tower. Thermocouples were positioned at 1, 2, 4, 8, 32, and 61 m on the same tower. Bivane and cup anemometer data were digitized and recorded at 2-s intervals during the effluent release. Each temperature reading was printed on a six-point recorder.

The field diffusion test was conducted November 30, 1967, from 1344 to 1415 MST. The sky was clear during the test period and 3 in. of snow, or more, covered the test area. The mean wind directions, wind speeds, and temperatures obtained on the grid III tower are listed in table 4.

Table 4. Average Winds and Temperatures at Grid III Tower

	Height (meters)							
	1	2	4	6	8	16	32	61
Wind speed (mps)	3.6		4.4	4.8		5.3		6.7
Wind direction (degrees)				248				250
Temperature (°C)	-2.3	-2.2	-2.2		-2.8		-2.9	-3.3

Figure 29 illustrates the patterns of $\chi\bar{u}/Q$ (source and wind speed normalized concentrations, χ) downwind from the release points. The solid lines represent iso-concentration contours for radioiodine; the dashed lines represent contours for uranine dye. All contour values are to be multiplied by 10^{-7}. Figure 29 reveals that it is questionable whether the plume axis remained on the grid much beyond 800 m downwind. As a consequence, very little can be said about comparisons beyond 800 m.

Examination of the total radioiodine collected by the samplers indicated a varied partition of radioiodine between the glass filters and carbon cartridges. Table 5 lists the percentage of radioiodine collected on glass filters by sampler arc and individual sampler positions (which were within the plume boundaries). The percentage of attachment to particulates varied from 60 to 70 percent near the plume boundary to 80 to 90 percent close to the plume center.

At sampler positions No. 1 through 7 on the 200-m arc, measured radioiodine concentrations were above background although uranine dye concentrations were not. In this region less than 20 percent of the iodine was collected on the glass filters. Thus suggests that the percentage of iodine attachment to particulates (uranine dye) increases as the uranine dye concentration increases.

Table 5. Percentage of Radioiodine Collected on Particulate Matter

Sampler Position	200 m	400 m	800 m	1600 m	3200 m
10	-	-	-	-	-
11	69	-	-	-	-
12	75	67	-	-	-
13	88	80	80	-	-
14	92	*	79	-	-
15	77	86	80	-	-
16	83	85	80	77	81
17	88	88	78	72	-
18	89	85	80	-	-
19	82	86	82	*	-
20	87	21	67	76	-
21	80	54	93	-	-

* High volume air sampler failure

The standard deviations of horizontal effluent concentrations (σ_y) were calculated from the second moments of the measured concentrations at 200, 400, and 800 m downwind. Table 6 lists the values of σ_y for both uranine dye and radioiodine.

Table 6. Standard Deviations of Lateral Effluent Concentrations (meters)

	200 m	400 m	800 m
Uranine Dye	23.89	47.03	98.69
Radioiodine	22.15	49.16	99.77

Comparisons of these σ_y values, which are not significantly different for the two tracers, with NRTS climatological σ_y values in figure 30 shows that the uranine dye and radioiodine σ_y values fall between the NRTS curves for class D (isothermal vertical temperature profile) and class C (weak temperature lapse). The slope of the observed σ_y values versus distance is different from the climatological curves which is not unexpected in the comparison of a single trial with averaged data. This difference would probably be significant only if continued to 3200 m or further.

Further inspection of values of $(\chi\bar{u}/Q)$ plotted in figure 29 shows that the patterns of normalized concentration are quite similar in shape over the entire sampling grid. The magnitudes of $(\chi\bar{u}/Q)$ are not equal, however. In fact, there seems to be a systematic difference which appears to grow with increasing distance downwind from the sources. Graphically, this tendency for a growing, systematic difference may be shown by plotting the ratio of $(\chi_p\bar{u}/Q)_U$ to $(\chi_p\bar{u}/Q)_I$ for each sampling arc, where χ_p is the peak measured concentration on the arc, and the subscripts U and I represent the quantities for uranine dye and radioiodine, respectively. This ratio versus distance is shown as the dashed line in figure 31. Another way of representing this systematic difference in $(\chi\bar{u}/Q)$ values is the ratio of normalized crosswind integrated concentrations, $(CIC/Q)_U/(CIC/Q)_I$. The ratio of CIC values is shown as the dotted line in figure 31. Both ratios have the same general slope, showing an increase of the ratio with downwind distance. The solid line represents the mean of the dashed and dotted curves. The dot-dash line extension of the mean curve indicates the general trend that must occur between the source (where the ratio equals 1) and 200 m downwind. The downwind (x) trend of the ratio (y) may be approximated by the parabola $y = 1 + \sqrt{.03x}$, where x is measured in meters.

In figure 32 measured peak values of $(\chi\bar{u}/Q)$ for uranine dye and radioiodine are compared with NRTS climatological curves for lapse and isothermal conditions. The curve for uranine dye parallels the Class C curve closely, in agreement with the calculated values of σ_y shown in figure 30. The curve of $(\chi\bar{u}/Q)$ for radioiodine is displaced significantly toward lower concentrations from the curve for uranine dye, extending slightly below the class A curve.

Before continuing further, the implications of an irregular release rate of radioiodine should be considered. Suppose the radioiodine release occurred as a single puff or as a short concentrated burst of effluent. Then, relative to the uranine dye, χ_p should be high, σ_y should be small, the direction of the plume center might differ or some combination of these should be evident. None of these three conditions is satisfied, however, and the release must not have been puff-like.

Suppose the radioiodine release were more like a number of puff releases superimposed on a more steady low rate of release. Relative to uranine dye, χ_p should be small, and σ_y should be large. This condition was not satisfied by σ_y although χ_p was smaller. Therefore, the radioiodine release must have been sufficiently similar to a steady release rate that any comparison with uranine dye need not correct for variations in radioiodine release rate during the test.

The differences in relative concentrations illustrated in figures 31 and 32 must reflect a real phenomenon, one developing primarily between the source and 200 m downwind. A simple rearrangement of the equation for concentration downwind from a continuous point source yields

$$\sigma_z = (Q/\chi\bar{u}\ \pi\sigma_y)\ \exp\left[-\frac{1}{2}\left(\frac{y^2}{\sigma_y^2}+\frac{h^2}{\sigma_z^2}\right)\right]. \qquad (11)$$

At the plume axis y = h = o and the exponential term equals 1. The right hand side of equation (11) is proportional to the mass flux away from the plane z = constant. Since σ_y was essentially the same for uranine dye and radioiodine, $\pi\sigma_y$ is a constant. Attaching a subscript to the terms in equation (9), with U denoting uranine dye and I radioiodine, and forming the ratio of iodine concentration to dye concentration provide

$$\frac{(\chi\bar{u}/Q_I)}{(\chi\bar{u}/Q_U} = \frac{(\sigma_z)_U}{(\sigma_z)_I} = \frac{F(z)_U}{F(z)_I}\ , \qquad (12)$$

where F(z) denotes the flux of effluent away from the horizontal plane through the height of the samplers, and (σ_z) is the net or effective standard deviation of vertical effluent concentration. From figure 31 one observes that the integrated effect of different vertical flux rates between the source and 200 m downwind results in a relative

mass flux or dispersion for radioiodine which is about four times the effective uranine dye vertical dispersion. This difference in effective vertical dispersion continues to increase but at a more gradual rate downwind through 800 m.

The four carbon fallout plates which were within the bounds of the plume received fallout that resulted in calculated disposition velocities averaging 0.65 cm/s. These velocities are in agreement with deposition velocities measured in previous CERT tests at the NRTS.

In conclusion, the observations may be summarized as follows:

Lateral dispersion at the height of the source (1 m above the ground) is almost identical for uranine dye and radioiodine. The slope of σ_y versus distance differs from climatological curves based on repeated field diffusion tests (of uranine dye) which were conducted on the same diffusion grid in previous years. The full significance and downwind extent of this difference in slope is not known.

The vertical flux of radioiodine within the first few hundred meters downwind of the source is approximately five times greater than the flux of uranine dye. This trend in vertical flux ratio follows a curve something like a parabola in which the effect increases most rapidly within the first 200 m of transport and then more gradually at distances beyond 200 m downwind.

Most of the radioiodine sampled from the effluent plumes was found attached to particulate matter. It is believed most of this particulate was uranine dye and the attachment occurred in the atmosphere prior to sampling.

Deposition of radioiodine measured on four carbon fallout plates between 200 and 3200 m downwind appears in agreement with deposition observed in past CERT field tests. Deposition within 200 m of the source was not measured. More deposition data are needed to strengthen or disprove the apparent agreement.

This field test answered a few questions, but raised many new ones, such as:

1) What physical process occurs during the first 200 m of transport that results in the vertical flux difference.?

2) Can anything be said about the deposition of the uranine itself in an absolute sense.

3) What is the downwind extent of this phenomenon?

4) Is the radioiodine really attached to a particulate in the atmosphere or was the radioiodine trapped by preloaded uranine dye in the glass fiber filter when the radioiodine was drawn through the high volume air sampler?

5) Is the process dependent upon the presence of particulates, such as uranine dye, in the atmosphere in excess of some minimum concentration?

Two, and possibly three, laboratory or field tests are under design to provide data for resolving these questions qualitatively and, in some instances, quantitatively.

3.0 REVIEW OF REACTOR SAFETY ANALYSIS REPORT

The Air Resources Laboratories in Silver Spring, Maryland, and the Field Office in Idaho have continued to take an active part in the review of reactor safety analysis reports as well as consultations with regard to the preparation of the reports. In addition, written comments have been prepared for the Division of Reactor Licensing through the Division of Reactor Development and Technology as follows:

1. Fort St. Vrain Nuclear Generating Station, Public Service Company of Colorado, Application for Construction Permit and Class 104 License, Amendment No. 3, dated July 10, 1967.

2. Tortuguero Nuclear Plant Site, Puerto Rico Water Resources Authority, Addendum No. 2, dated July 12, 1967.

3. Pilgrim Nuclear Power Station, Design and Analysis Report, Volumes I, II, and III, dated June 23, 1967.

4. Peach Bottom Atomic Power Station Units No. 2 and 3, Philadelphia Electric Company, Preliminary Safety Analysis Report, Supplement No. 1, dated July 12, 1967.

5. Zion Station Units 1 and 2, Commonwealth Edison Company, Preliminary Safety Analysis Report, Volumes I and II, dated July 12, 1967, and Amendment No. 1, dated August 15, 1967.

6. Easton Nuclear Station, Niagara Mohawk Power Corporation, Preliminary Safety Analysis Report, Volume I, dated August 1, 1967.

7. Diablo Canyon Site, Pacific Gas and Electric Company, Preliminary Safety Analysis Report, Third Supplement, dated July 31, 1967.

8. Argonne Advanced Research Reactor, Preliminary Safety Analysis Report, Supplement 3, dated July 18, 1967.

9. Surry Power Station Units 1 and 2, Virginia Electric and Power Company, Preliminary Safety Analysis Report, Amendment No. 3, dated August 24, 1967.

10. Southwest Experimental Fast Oxide Reactor, Facility Description and Safety Analysis Report, Volumes I and II, dated July 24, 1967.

11. Cooper Nuclear Station, Consumers Public Power District, Preliminary Safety Analysis Report, Volumes I, II and III, dated July 27, 1967.

12. Fort St. Vrain Nuclear Generating Station, Public Service Company of Colorado, Application for Construction Permit and Class 104 License, Amendment No. 4, dated August 28, 1967.

13. Oyster Creek Nuclear Power Plant Unit No. 1, Jersey Central Power and Light Company, Facility Description and Safety Analysis Report, Amendment No. 11, dated August 30, 1967, and Amendment No. 13, dated September 7, 1967.

14. Crystal River Units 3 and 4 Nuclear Generating Plant, Florida Power Corporation, Preliminary Safety Analysis Report, Volume 1, dated August 10, 1967.

15. Pilgrim Nuclear Power Station, Design and Analysis Report, Amendment No. 2, dated October 11, 1967.

16. Fort Calhoun Station - Unit No. 1, Omaha Public Power District, Facility Description and Safety Analysis Report, Supplement No. 3, dated September 25, 1967, and Supplement No. 5, dated September 29, 1967.

17. Prairie Island Nuclear Generating Plant, Units 1 and 2, Northern States Power Company, Facility Description and Safety Analysis Report, Volumes I, II, and III, dated August 30, 1967.

18. Kewaunee Nuclear Power Plant, Wisconsin Public Service Corporation, Facility Description and Safety Analysis Report, Volumes I and II, dated August 23, 1967.

19. Fort St. Vrain Nuclear Generating Station, Public Service Company of Colorado, Application for Construction Permit and Class 104 License, Amendment No. 5, dated October 11, 1967.

20. Nine Mile Point Nuclear Station, Niagara Mohawk Power Corporation, Final Safety Analysis Report, dated June 1967, and Amendment No. 3, dated July 14, 1967.

21. Main Yankee Atomic Power Station, Main Yankee Atomic Power Company, Preliminary Safety Analysis Report, Volumes I and II, dated October 11, 1967.

4.0 PUBLICATIONS

1. Angell, J. K. and D. H. Pack (1967), "Helical circulations in the planetary boundary layer," Phys. Fluids 10(9), Part II, 226-229.

2. Dickson, C. R., ed. (1967), "Meteorology for the loss of fluid test reactor," Progress Report, January 1966 - January 1967, USAEC Idaho Operations Office, Document IDO-12059.

3. Hass. W. A., W. H. Hoecker, D. H. Pack, and J. K. Angell (1967), "Analysis of low-level, constant volume balloon (tetroon) flights over New York City," Quart. J. Roy. Meteorol. Soc. 93(398), 483-493.

4. Slade, D. H. (1967), "Modeling air pollution in the Washington, D. C. to Boston megalopolis," Science 157(3794), 1304-1307.

5. Van der Hoven, I. (1967), "Atmospheric transport and diffusion at coastal sites," Nucl. Safety 8(5), 490-499.

5.0 LABORATORY PERSONNEL

5.1 Silver Spring, Maryland

Abram Bernstein, meteorologist, was granted a second-year extension of his scholarship for graduate training at the University of Washington.

5.2 National Reactor Testing Station, Idaho

Norman Ricks and Jack Simonds, student summer employees, returned to college in September.

Daunna Walker entered on duty December 6 as a temporary secretary, filling the position of the regular secretary who was absent because of extended illness.

Harry Zimmerman entered on duty August 31 as a meteorological technician, but due to a sudden death in his family, had to rejoin his family in Phoenix.

Earl Markee, meteorologist, began a one-year scholarship for graduate training at the University of Utah in September.

6.0 REFERENCES

Blackadar, A. K., H. A. Panofsky, P. E. Glass, and J. F. Boognard (1967), "Determination of the effect of roughness change on the wind profile," Phys. Fluids, 10(9), Part II, S209.

Cooley, J. W., P. A. W. Lewis, and P. D. Welch (1967), "The fast fourier transform algorithm and its application," JBM Res. Paper, Watson Research Center, 157.

Lund, Iver A. (1963), "Map-pattern classification by statistical methods," J. Appl. Meteorol. 2, 56-65.

Pasquill, Frank (1967), "The vertical component of atmospheric turbulence at heights up to 1200 m," Atmospheric Environ. 1, 441-450.

Rao, C. R., (1952), "Advanced Statistical Methods in Biometric Research" (Wiley, New York).

Van der Hoven, Isaac (1957), "Power spectrum of horizontal wind speed in the frequency range from 0.0007 to 900 cycles per hour," J. Meteorol. 14, 160.

Yanskey, G. R., E. H. Markee, Jr., and A. P. Richter (1966), "Climatolography of the National Reactor Testing Station," U. S. Atomic Energy Commission, IDO-12048, Idaho Falls, Idaho.

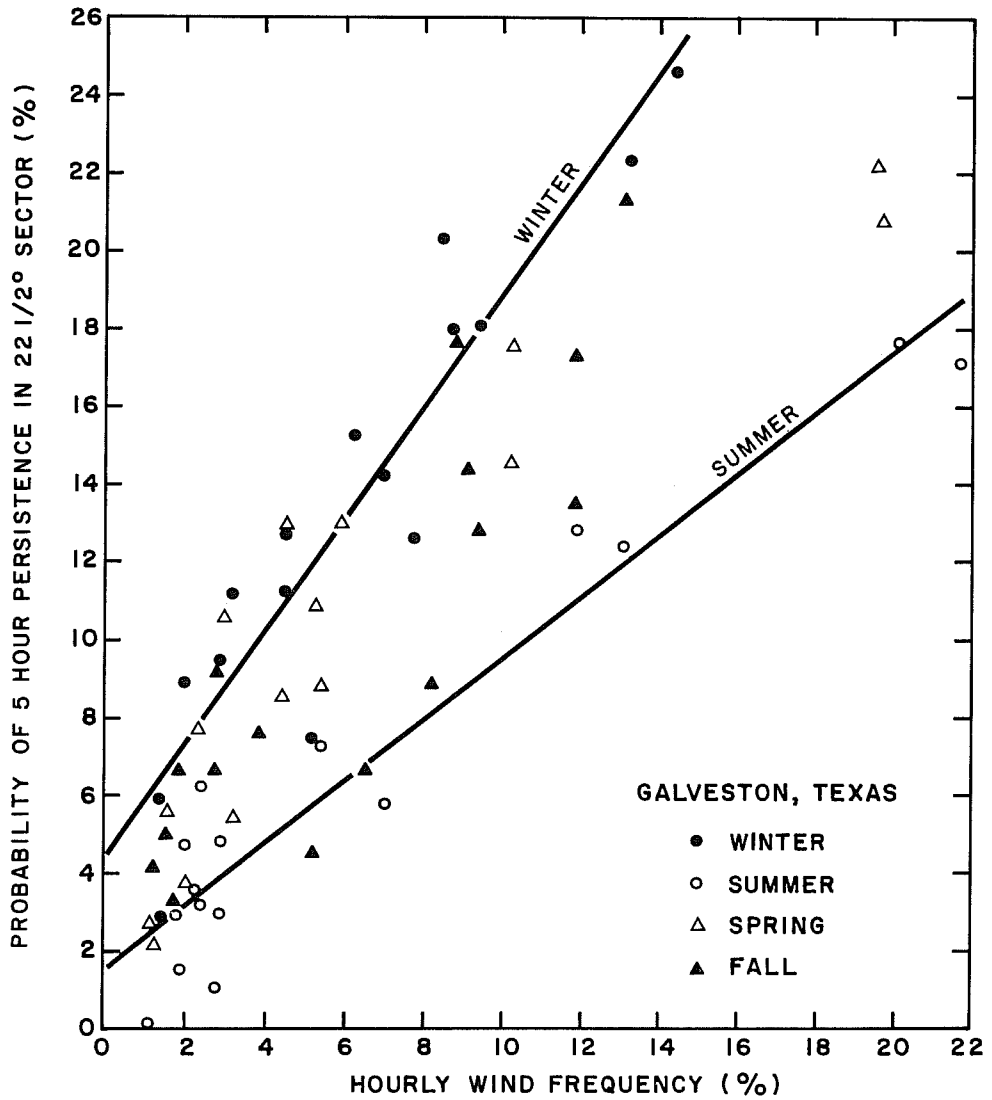

Figure 1. Relationship of wind direction frequency and persistence for Galveston, Texas.

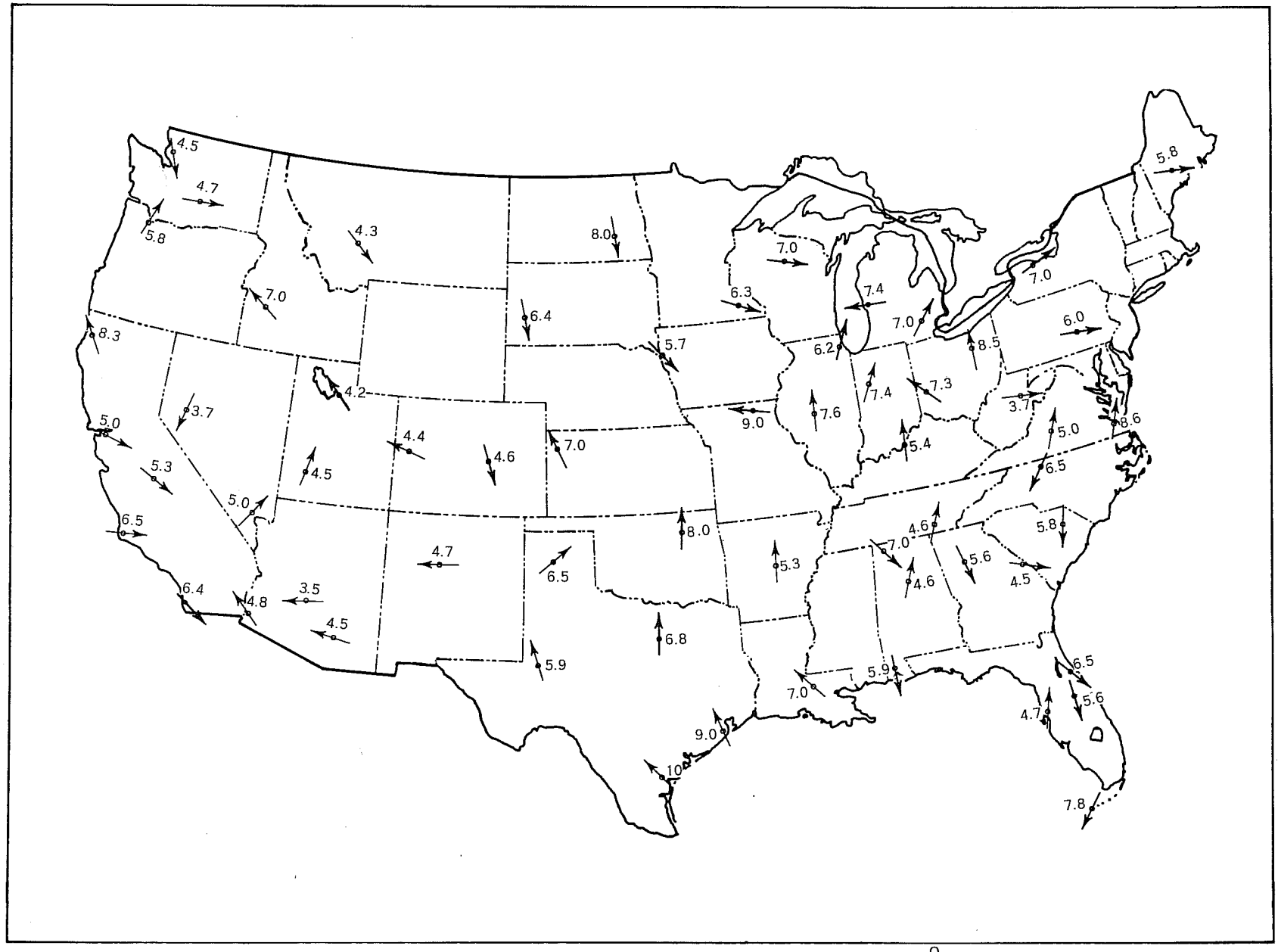

Figure 2. Highest hours at 10 percent probability of wind persistence in a 22 1/2° sector centered on the indicated direction.

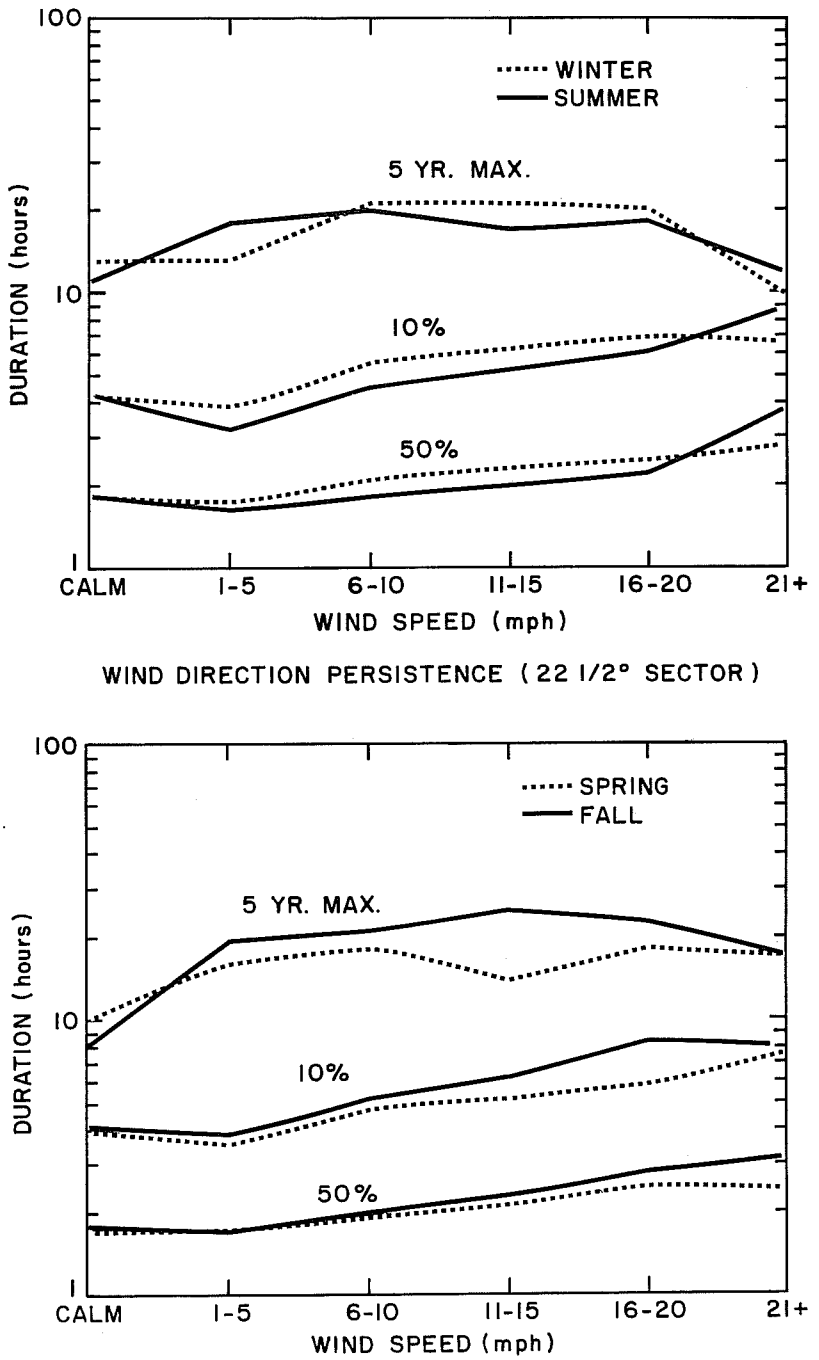

Figure 3. Wind direction persistence in a 22 1/2° sector as a function of speed for Daytona Beach, Florida.

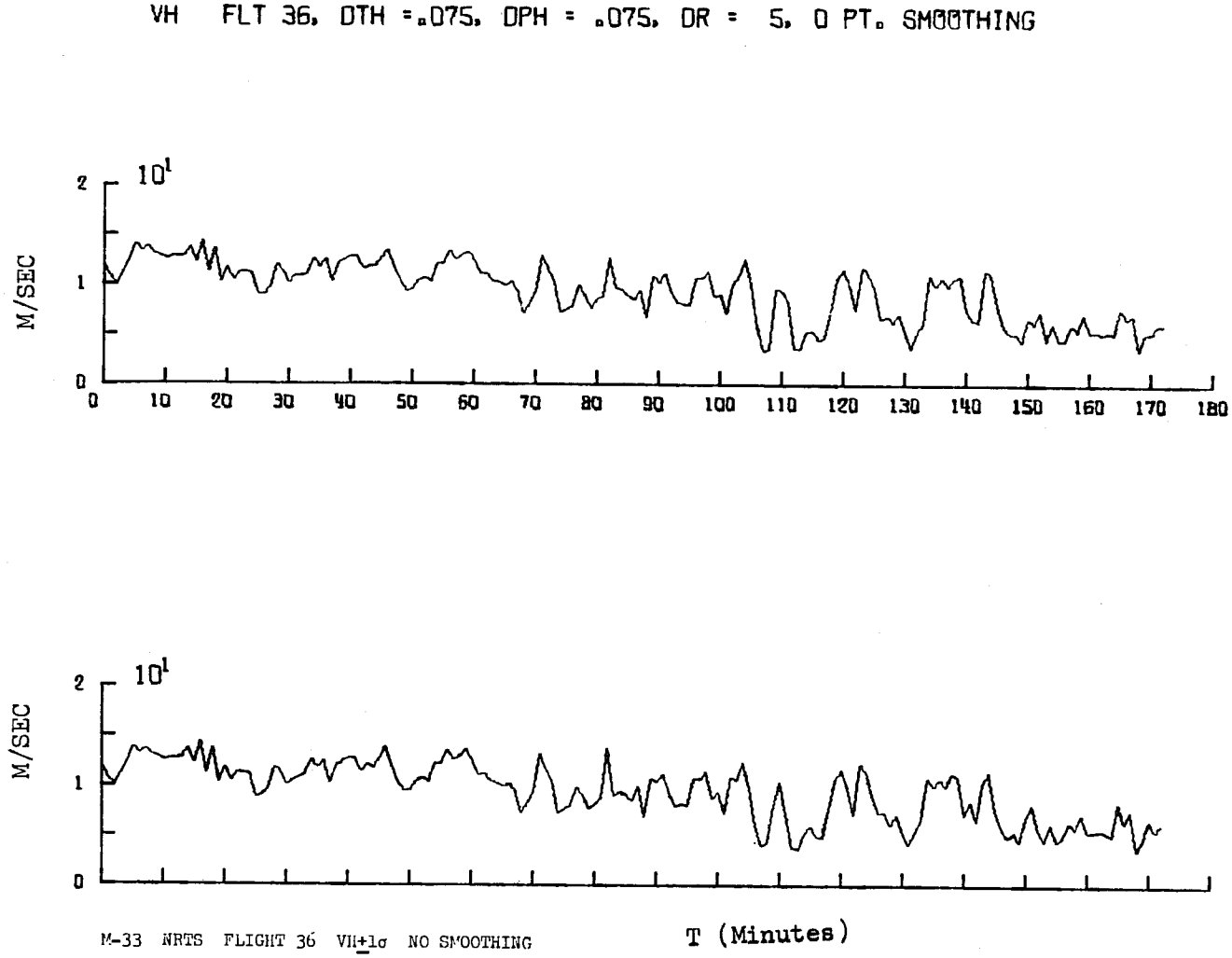

Figure 4. Horizontal velocity trace and corresponding $\pm$ 1σ error trace (lower graph).

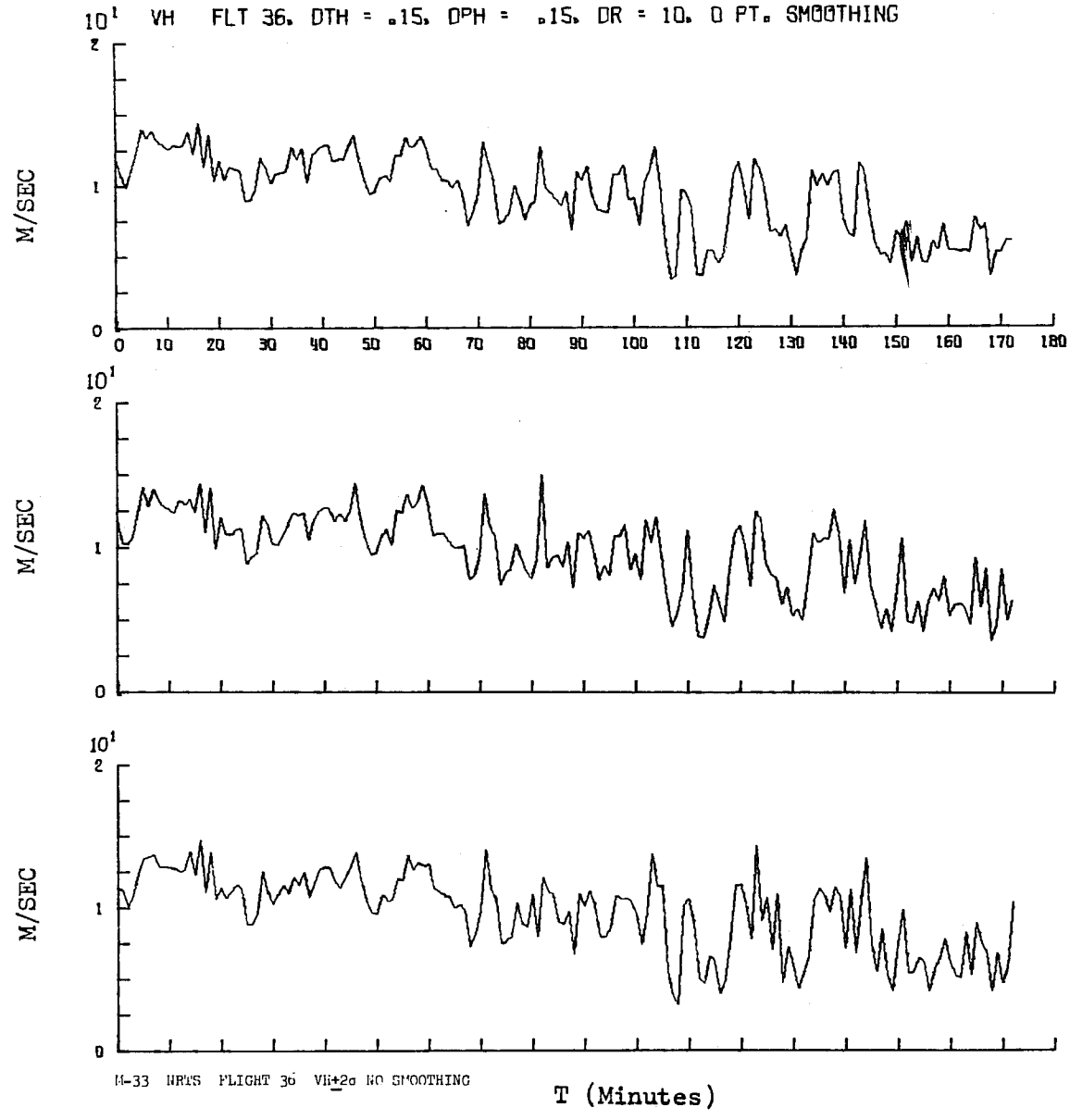

Figure 5. Horizontal velocity trace and corresponding $\pm 2\sigma$ error traces(two lower graphs).

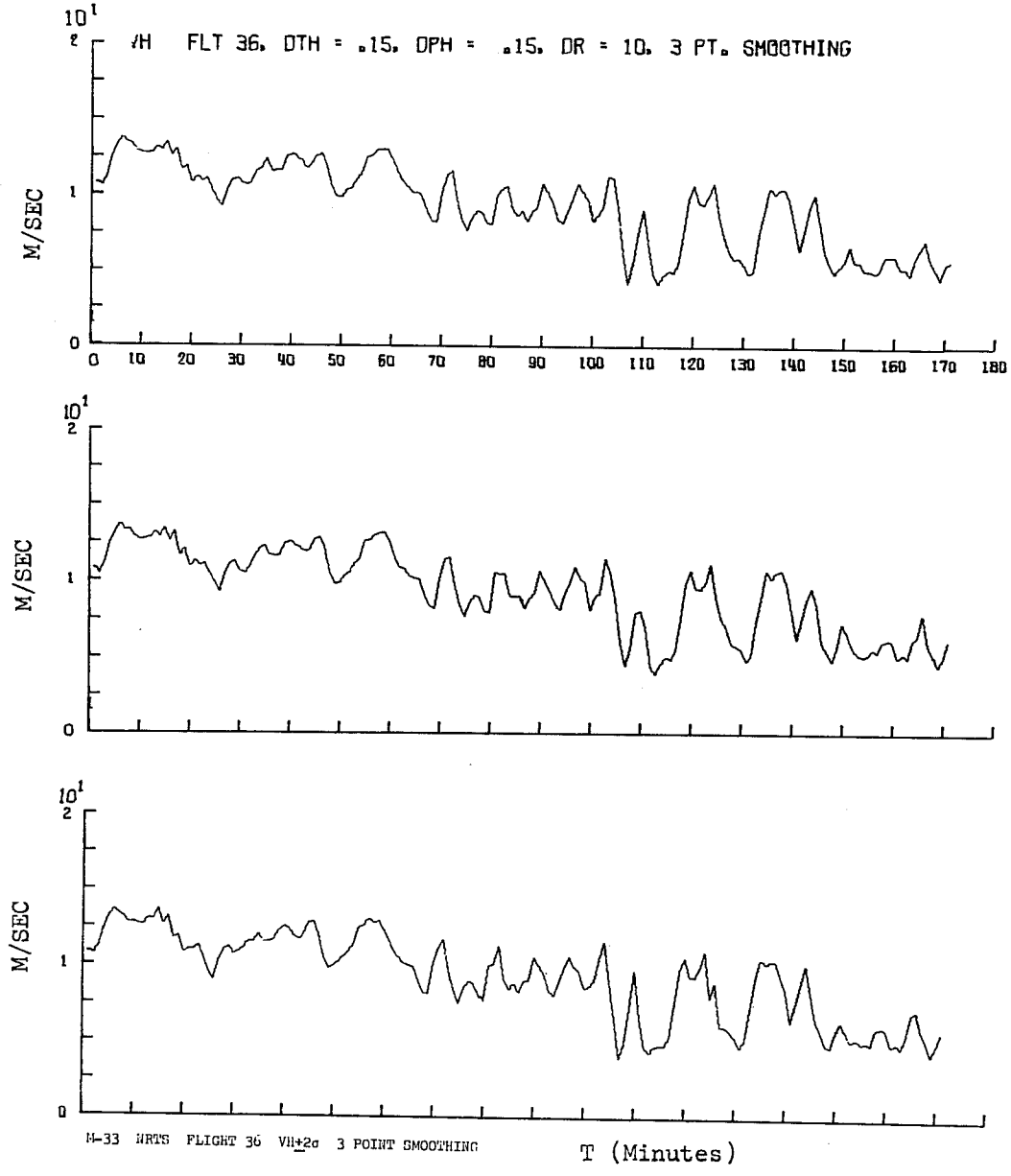

Figure 6. Horizontal velocity trace for a three-point running average and corresponding $\pm$ 2σ error traces (two lower graphs).

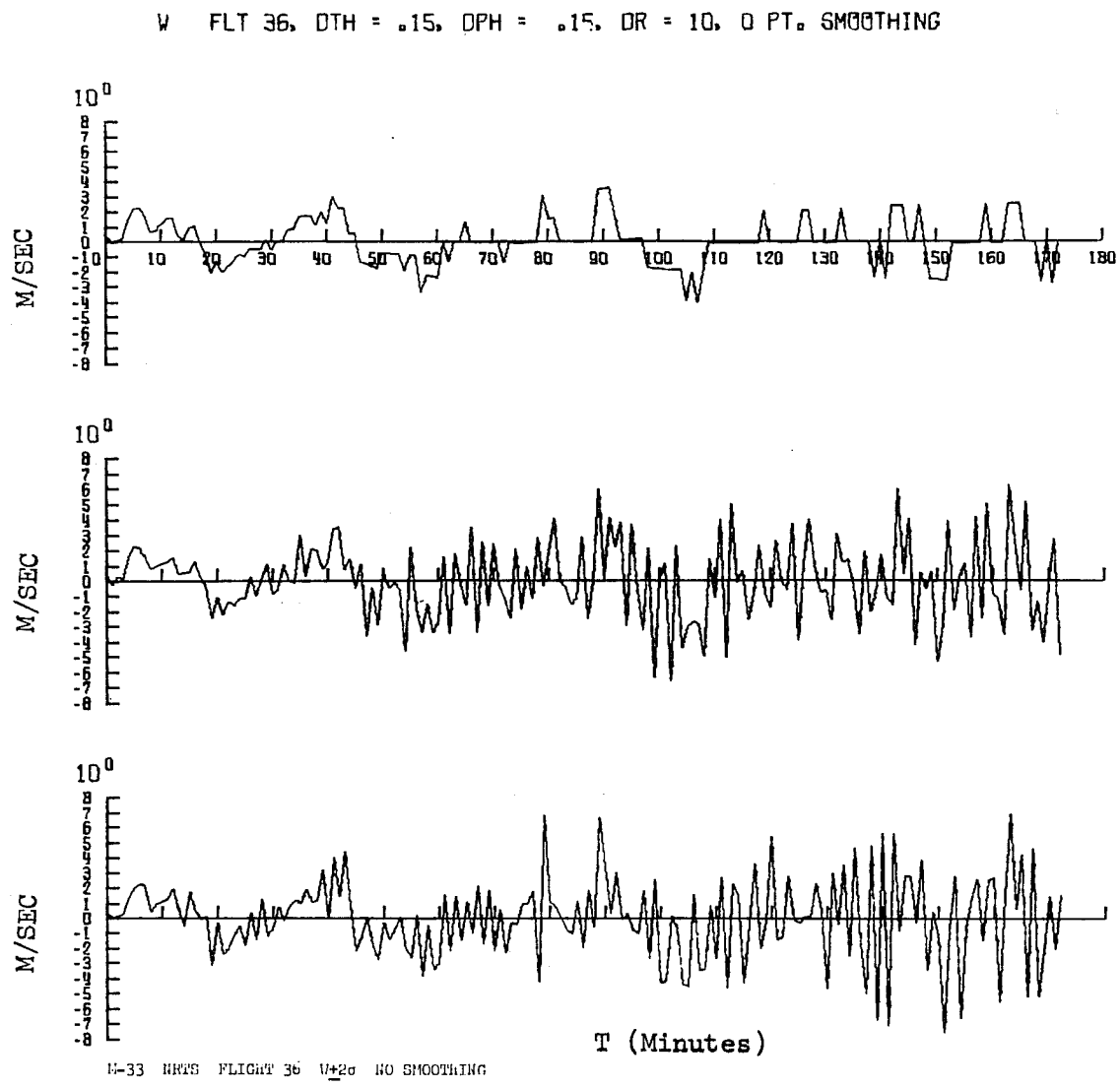

Figure 7. Vertical velocity trace and corresponding $\pm$ 2σ error traces (two lower graphs).

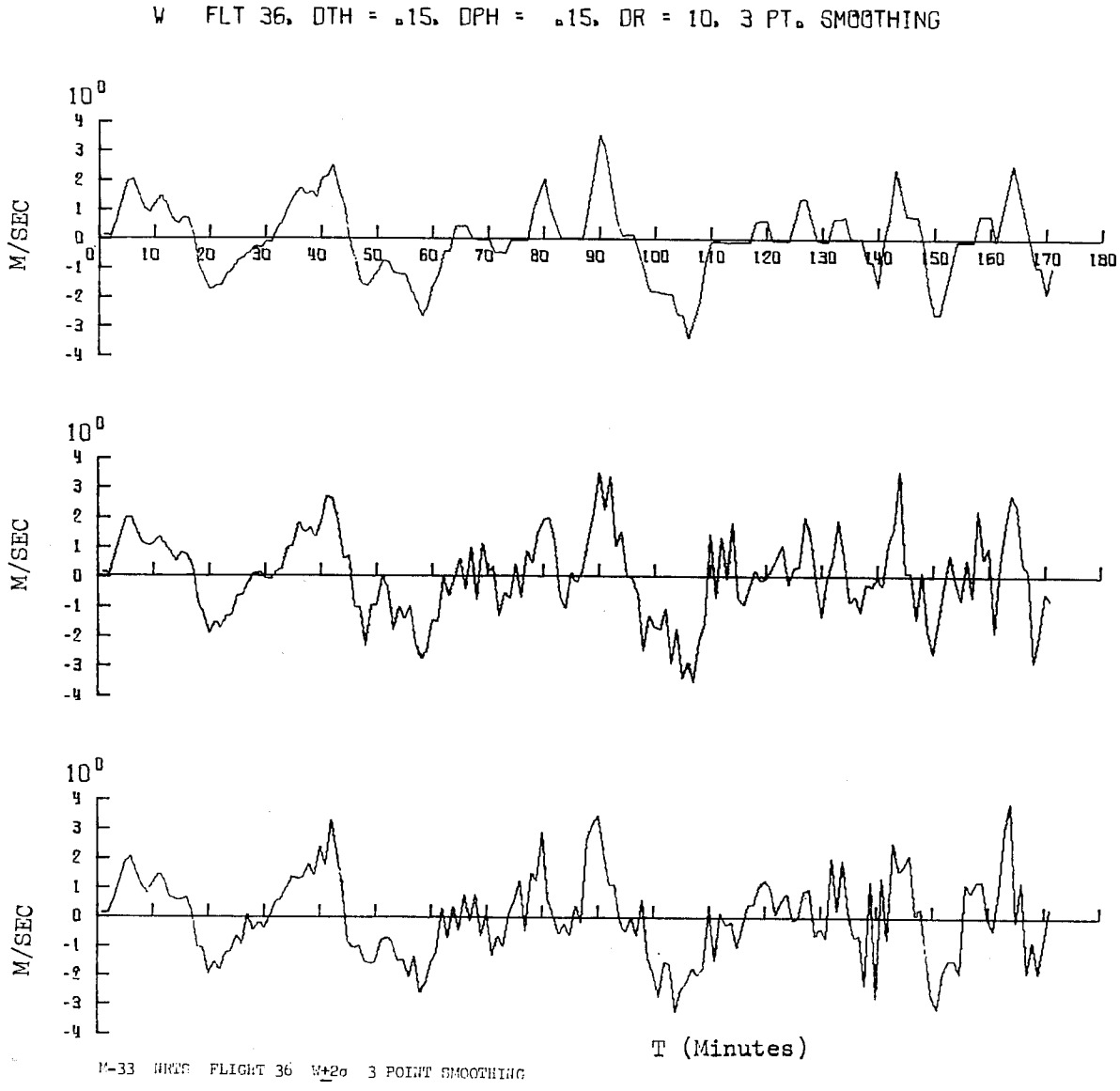

Figure 8. Vertical velocity trace for a three-point running average and corresponding $\pm 2\sigma$ error traces (two lower graphs).

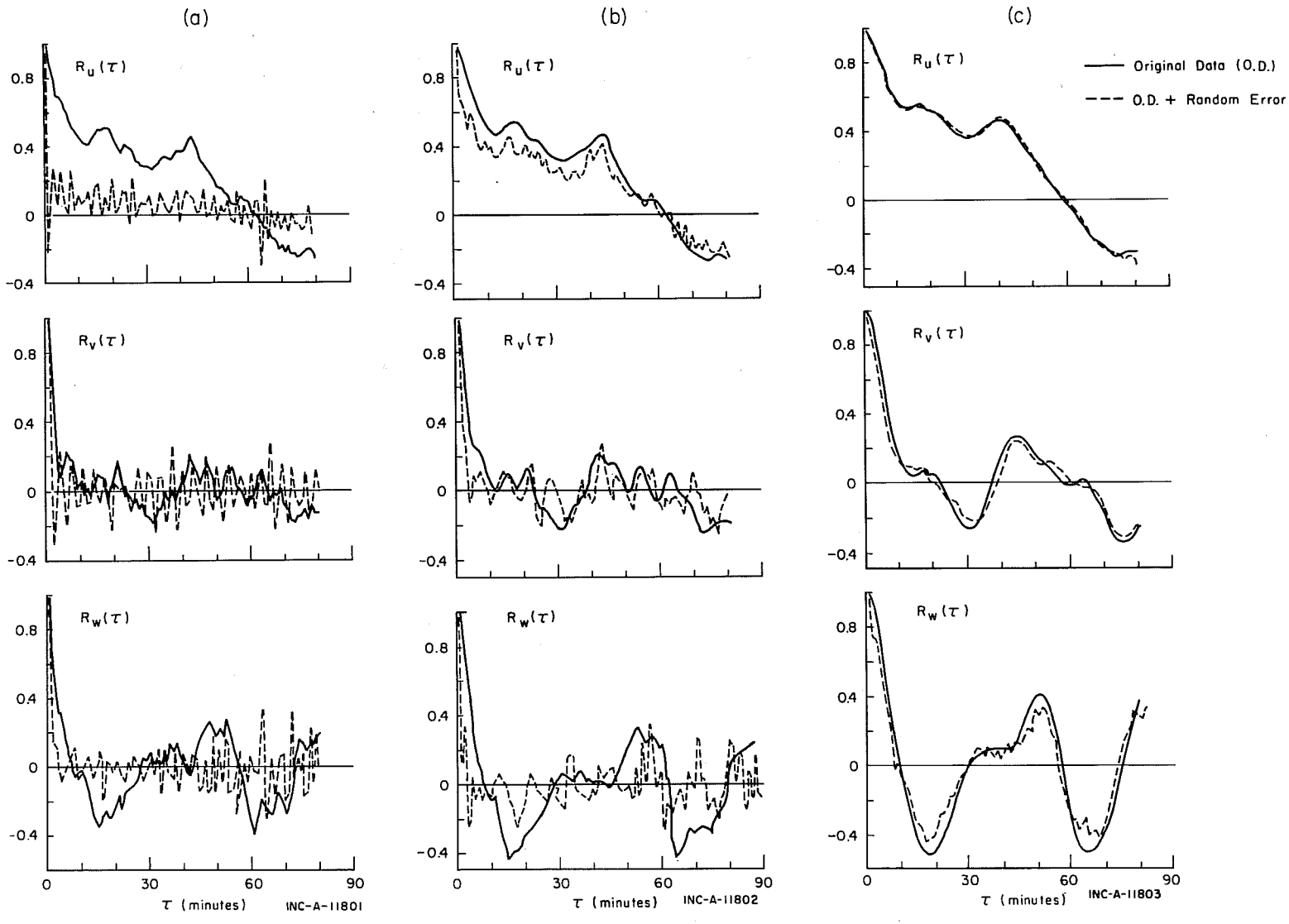

Figure 9. Autocorrelation functions for the u, v, and w components of velocity for no smoothing (a), three-point running average (b), and seven-point running average (c), and corresponding $\pm$ 2σ error traces (two lower sets of graphs).

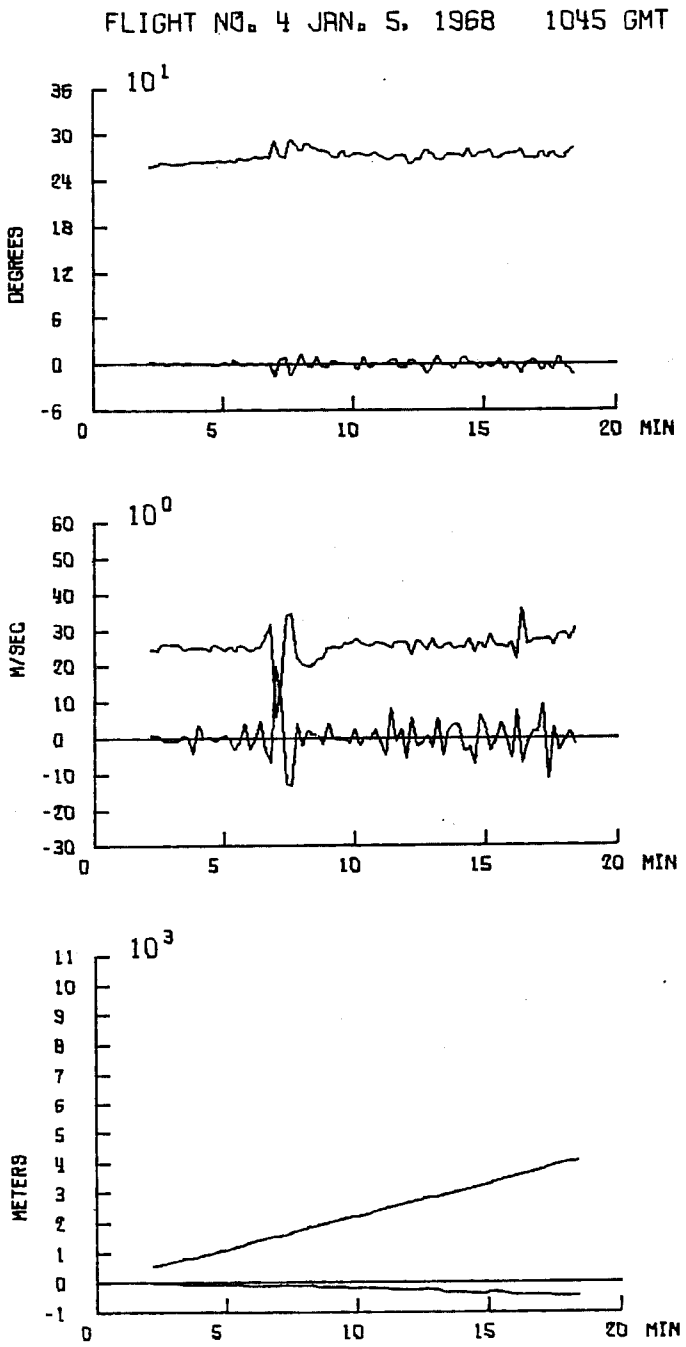

Figure 10. Balloon direction, velocity, and height, as computed from the tracking data of a WF44S radar (upper curve in each graph) and the corresponding deviation of the tracking data of a WF3 radar (lower curves).

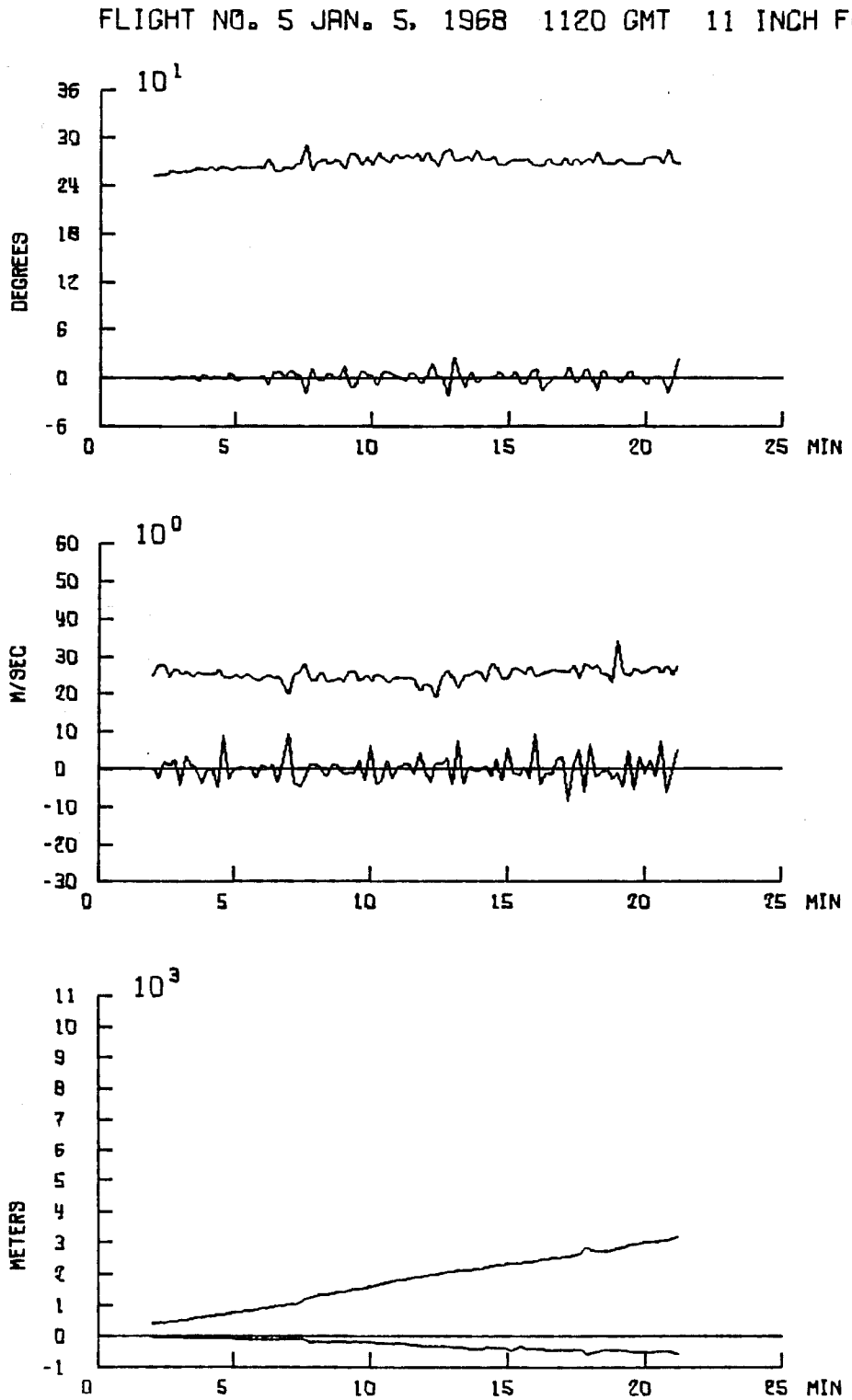

Figure 11. Balloon direction, velocity, and height, as computed from the tracking data of a WF44S radar (upper curve in each graph) and the corresponding deviation of the tracking data of a WF3 radar (lower curves).

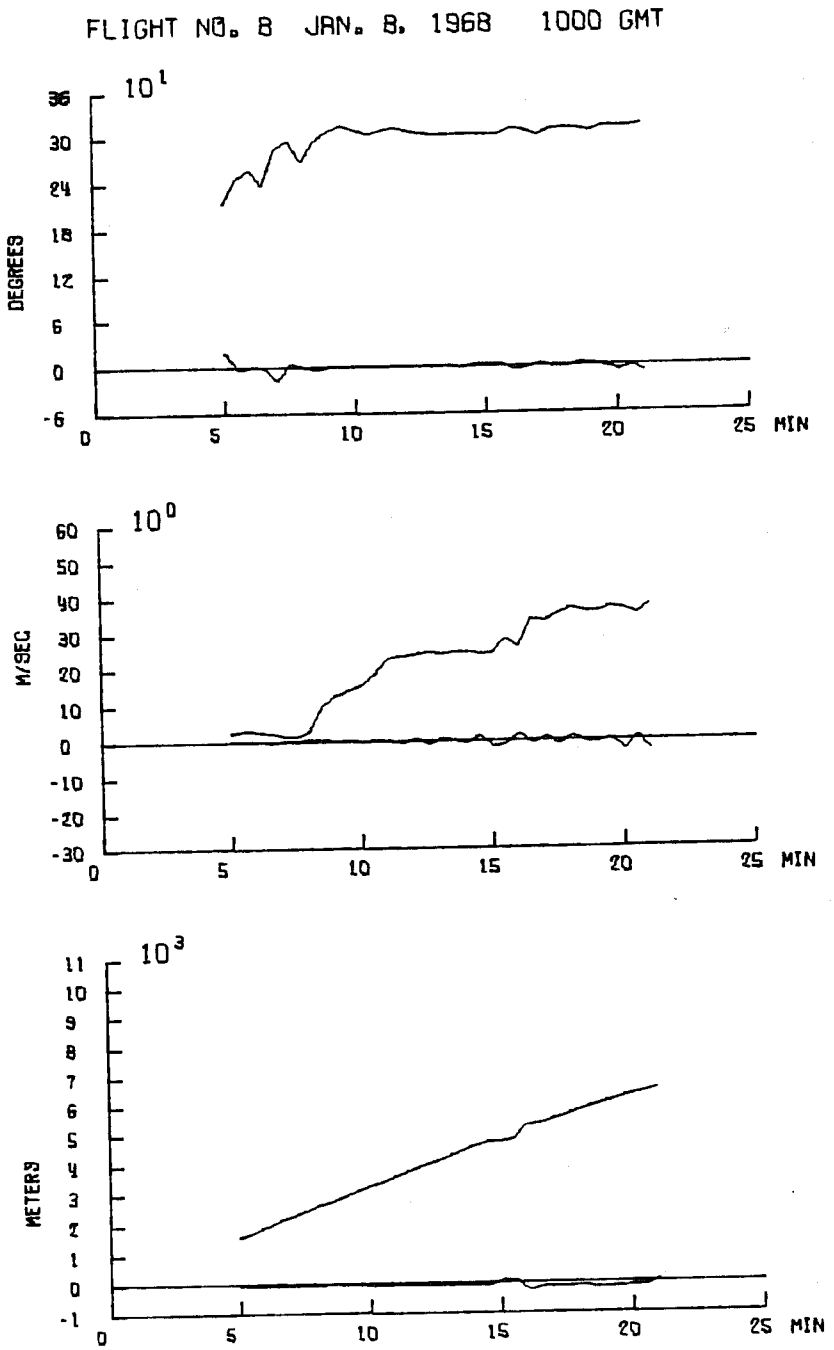

Figure 12. Balloon direction, velocity, and height, as computed from the tracking data of a WF44S radar (upper curve in each graph) and the corresponding deviation of the tracking data of a WF3 radar (lower curves).

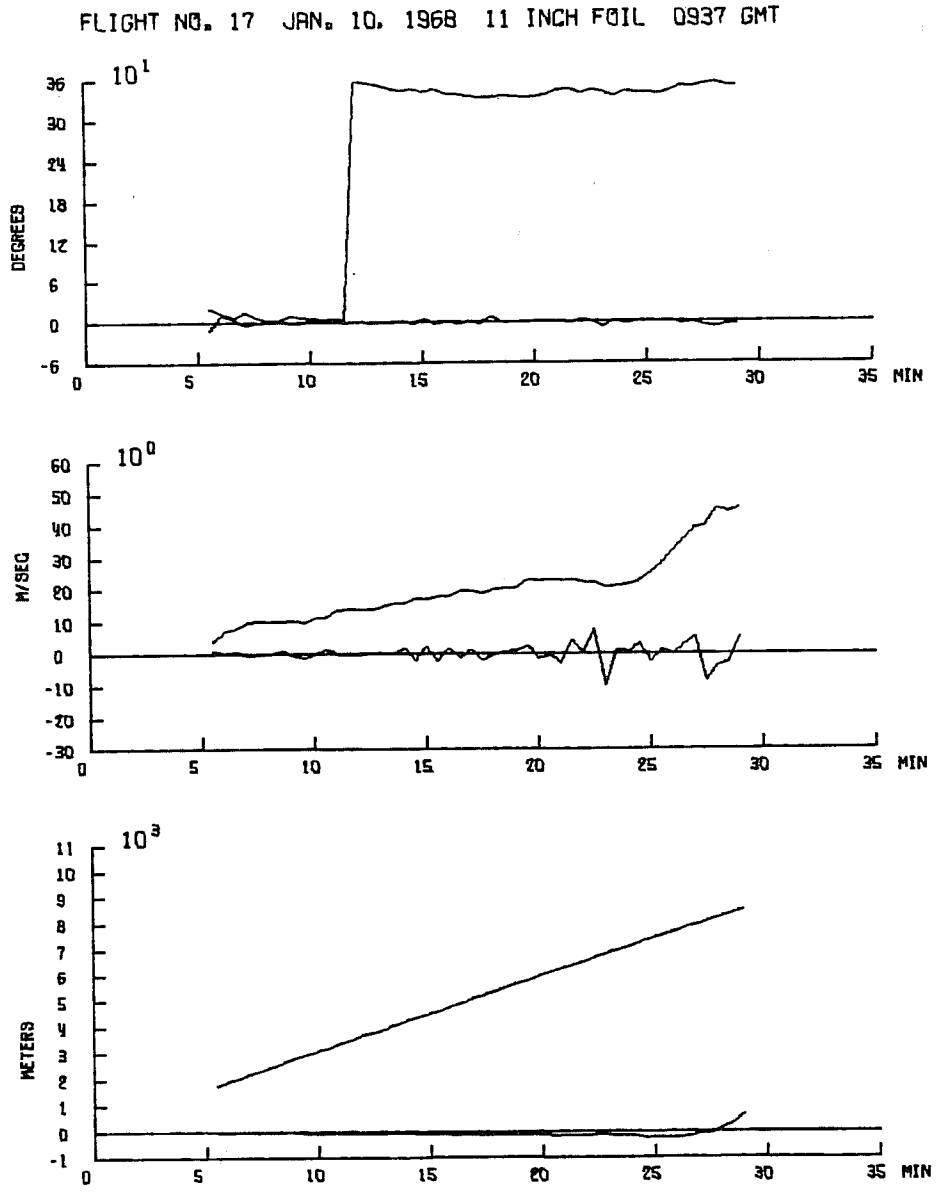

Figure 13. Balloon direction, velocity, and height as computed from the tracking data of a WF44S radar (upper curve in each graph) and the corresponding deviation of the tracking data of a WF3 radar (lower curves).

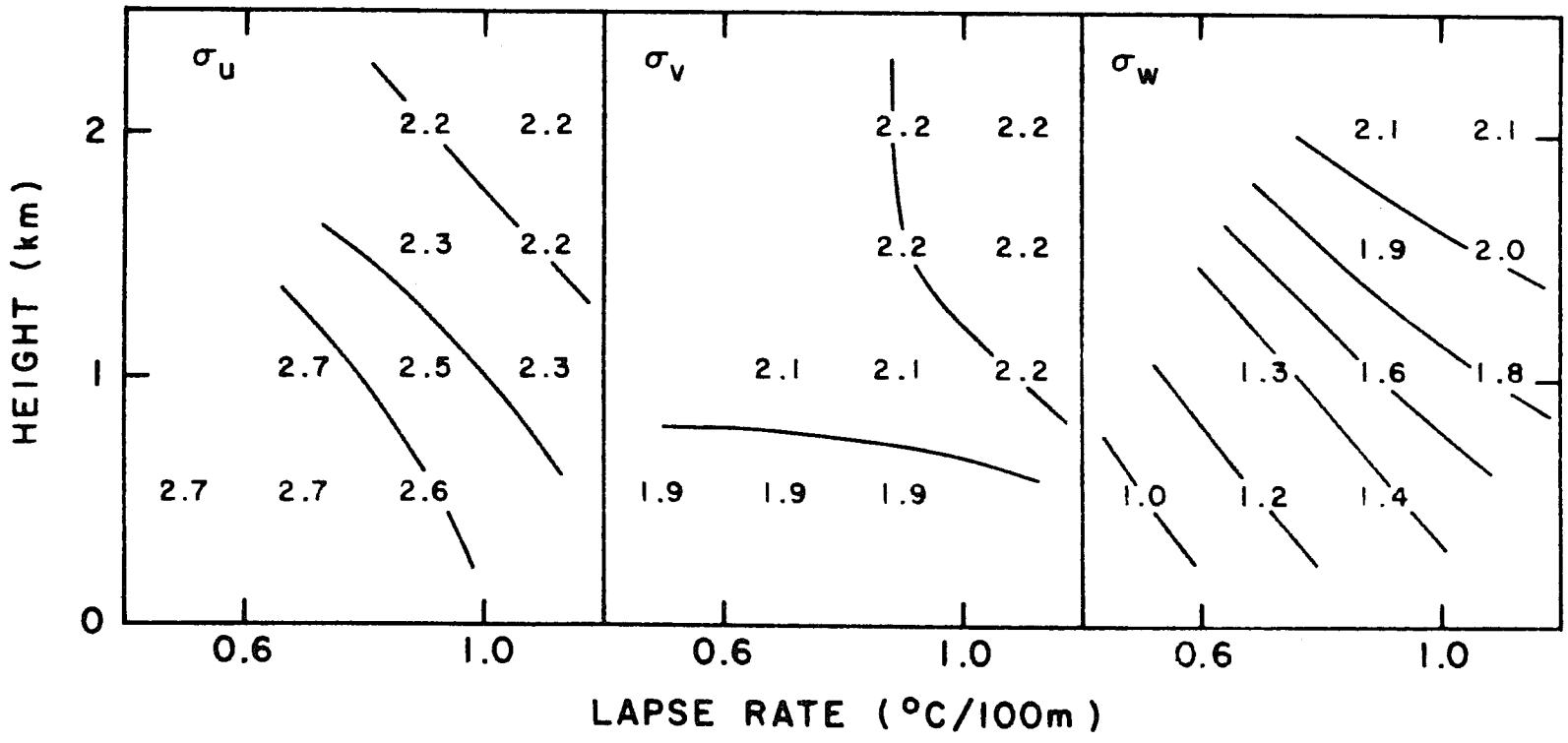

Figure 14. Variation with height and lapse rate of rms longitudinal (left), lateral (center), and vertical (right) velocity based on NRTS tetroon flights during one summer. Units are in ms^{-1}.

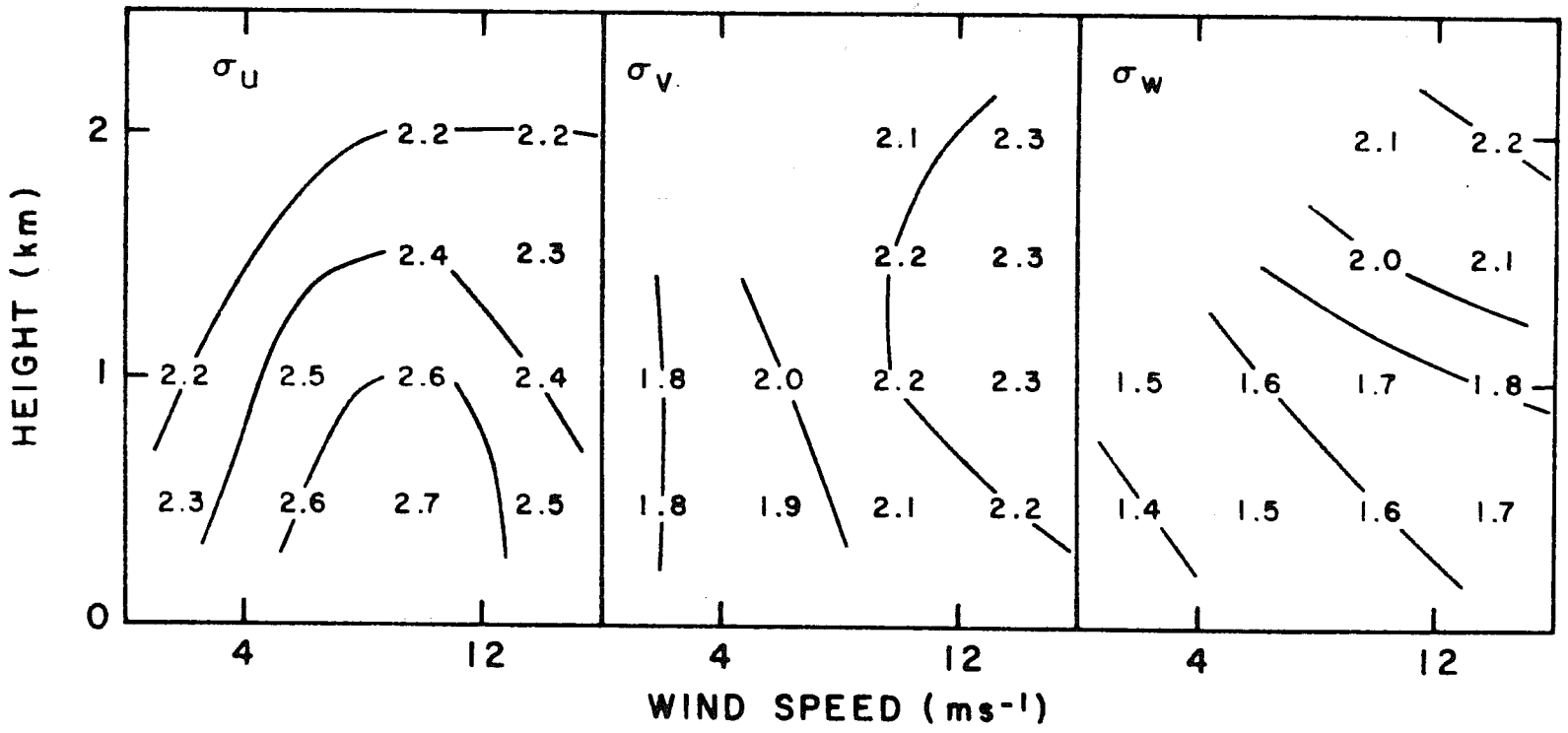

Figure 15. Variation with height and wind speed of rms velocity components in ms^{-1}, based on summer tetroon flights.

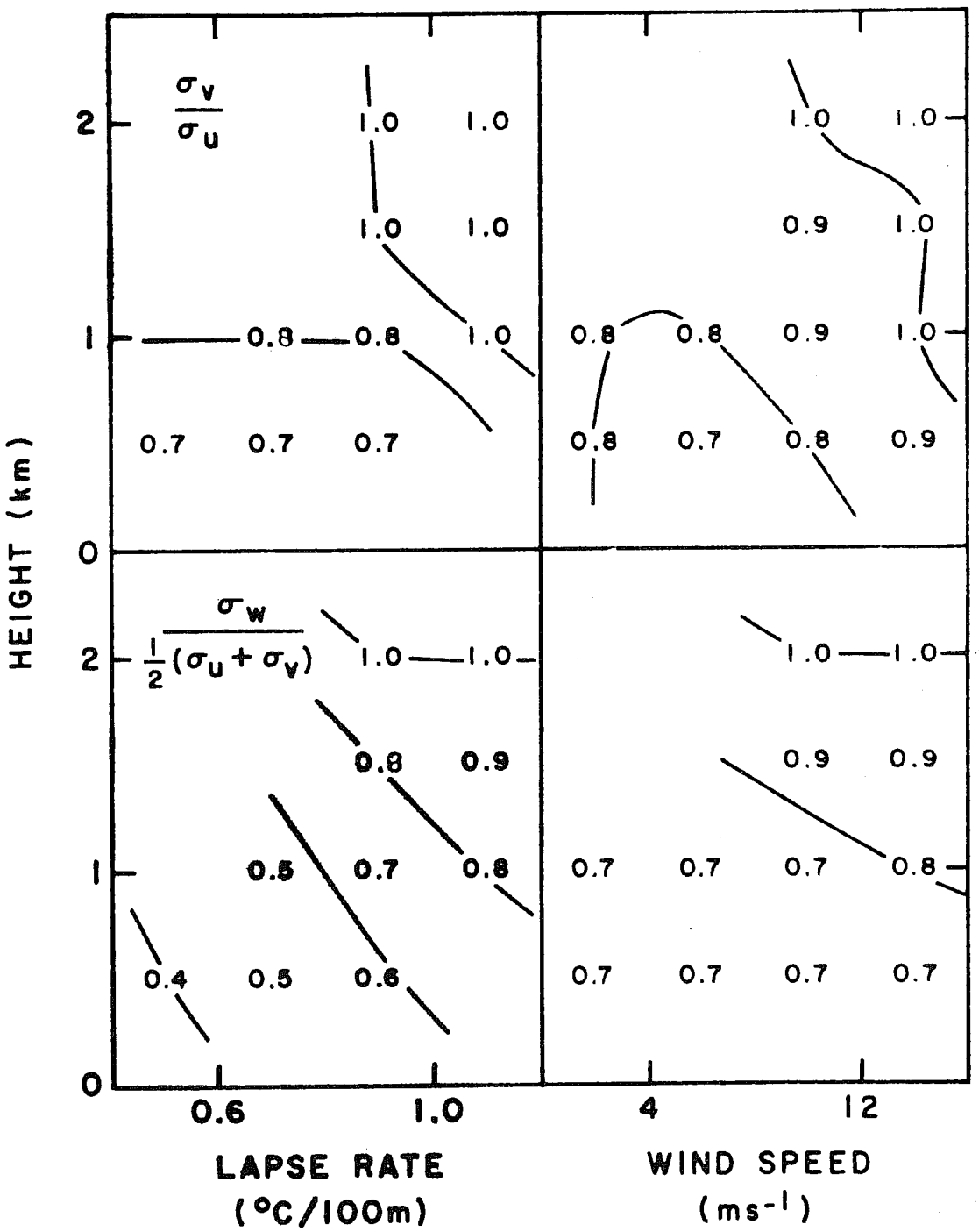

Figure 16. Summertime variation with height, lapse rate, and wind speed of ratio of rms lateral and longitudinal velocities (top) and vertical and average of horizontal component velocities (bottom).

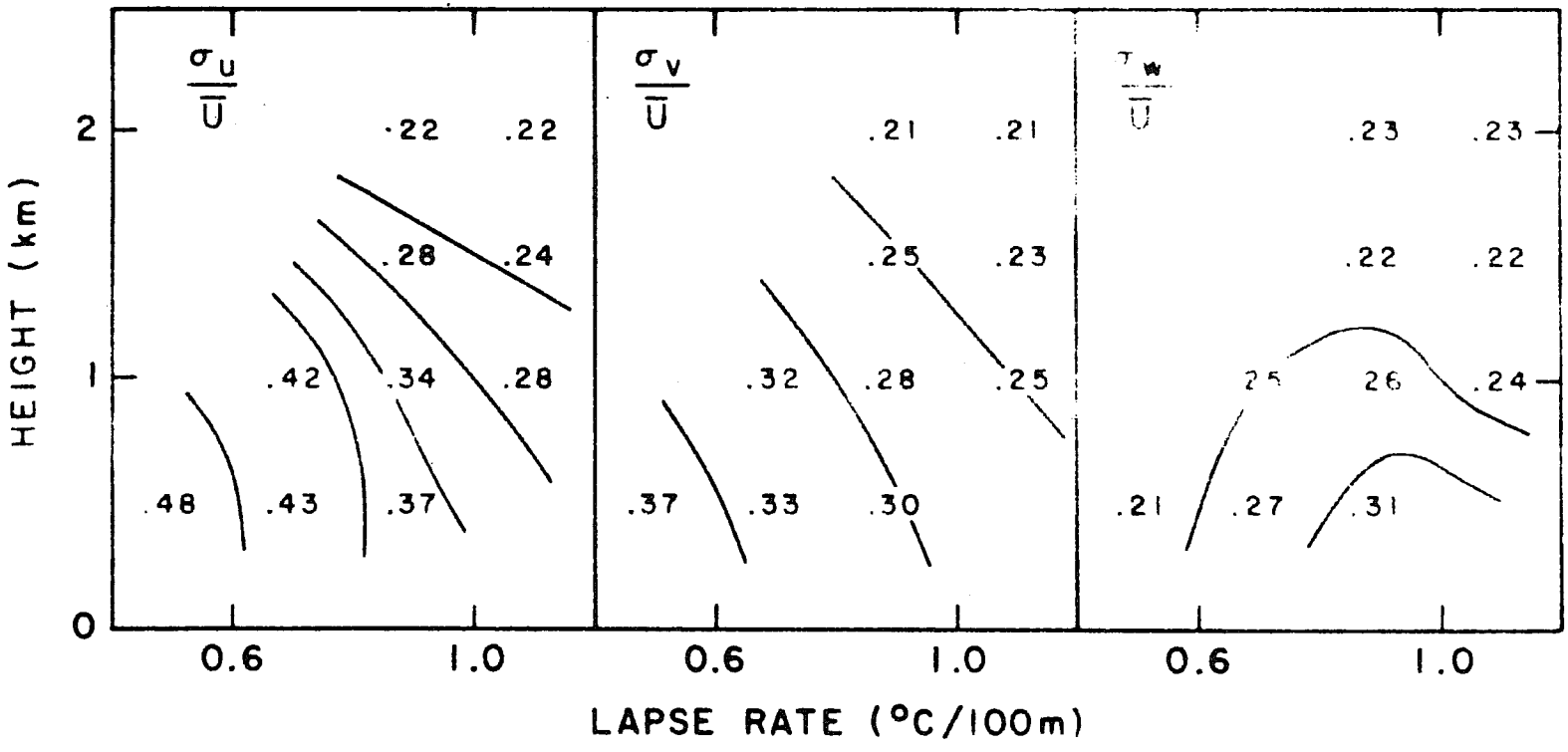

Figure 17. Variation of turbulence intensities with height and lapse rate in summer.

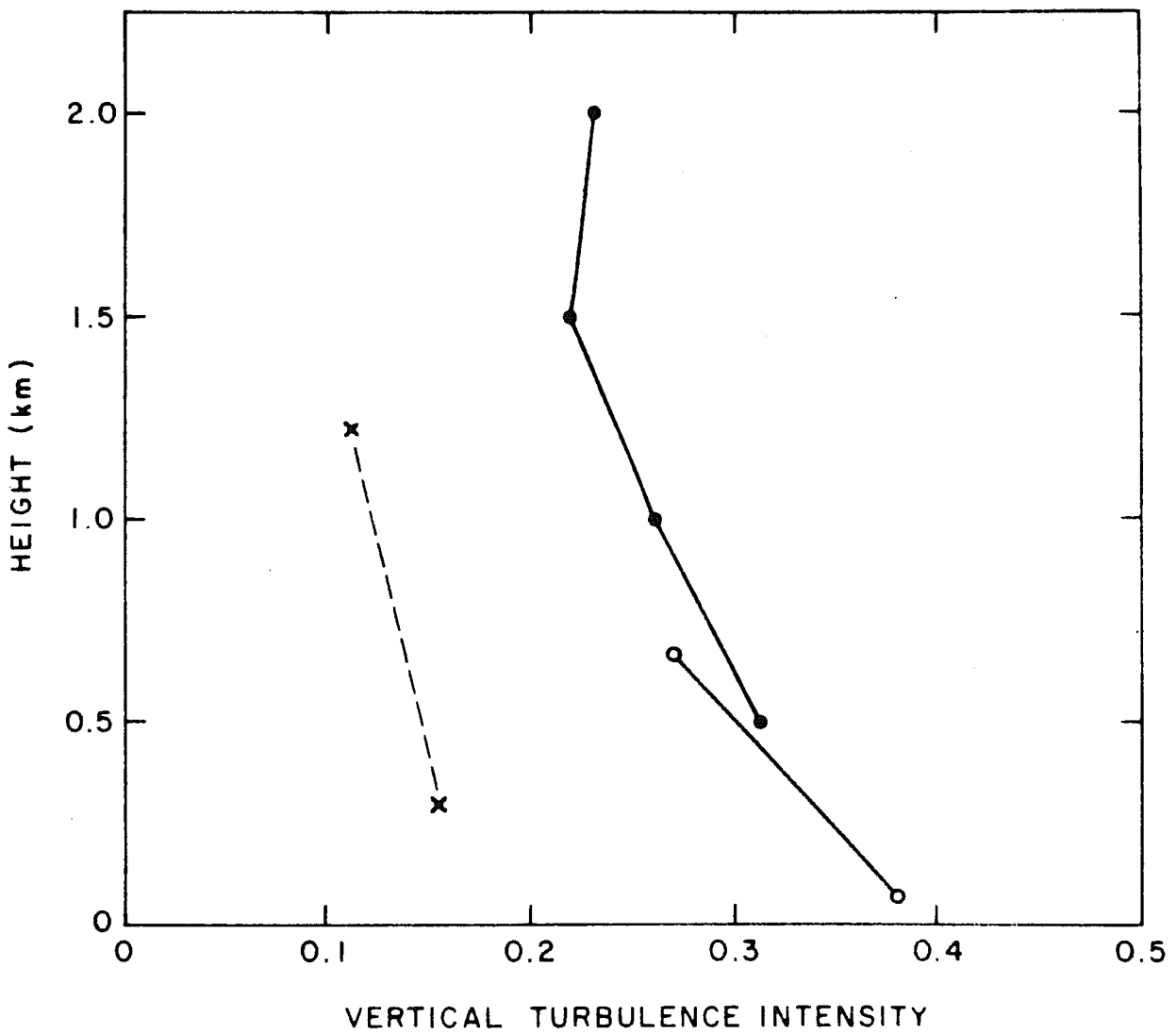

Figure 18. Height variation of vertical turbulence intensity in near-neutral conditions as obtained from fig. 17 and from tetroon flights throughout the year (solid lines with circles and dots, respectively) and from Pasquill's Cardington data (dashed line).

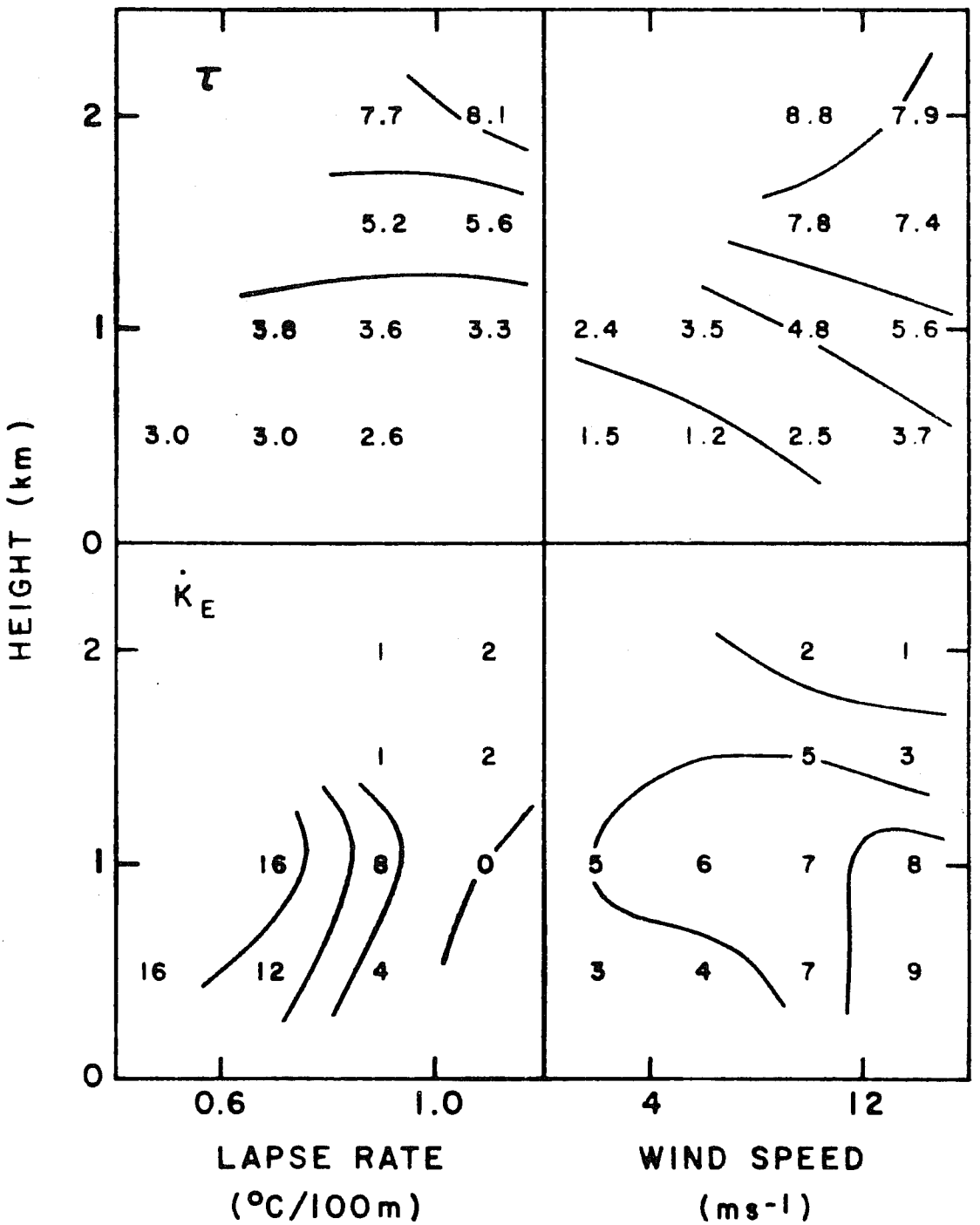

Figure 19. Summertime variation with height, lapse rate, and wind speed of vertical momentum flux (top), and rate of production of eddy kinetic energy from the mean sheared flow (bottom). Units are dynes/cm^2 and cm^{2}s^{-3}, respectively.

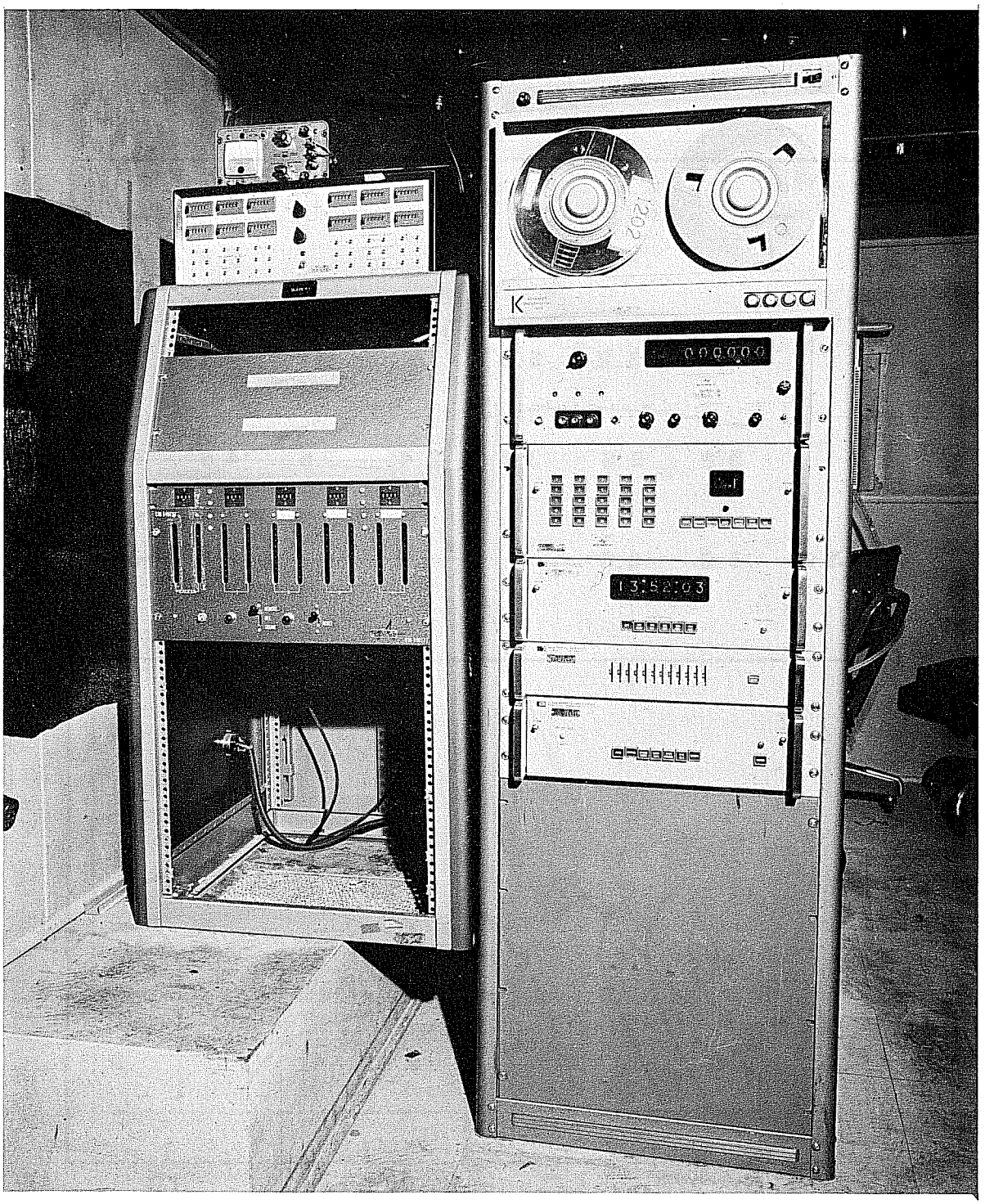

Figure 20. Hewlett-Packard Model 2010J Digital System.

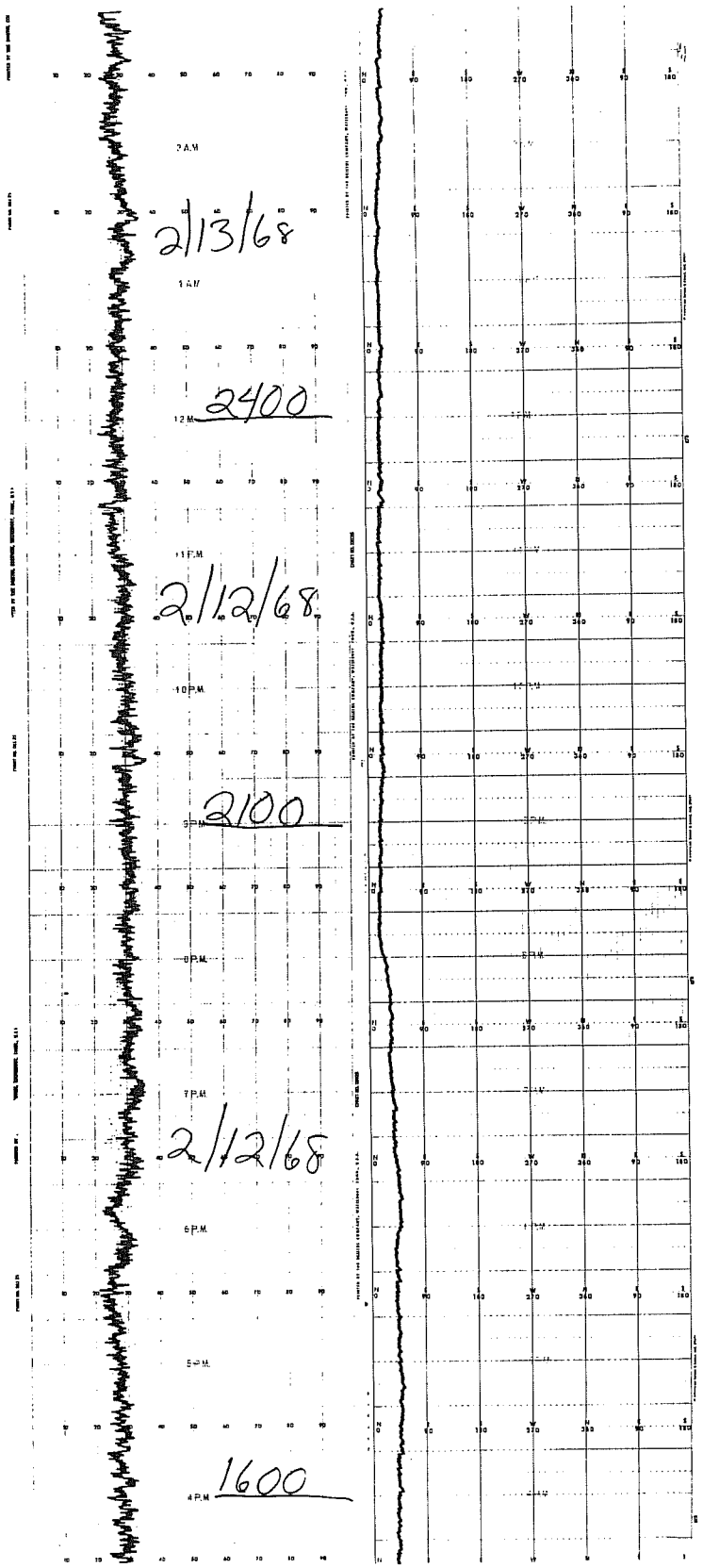

Figure 21. Sample of strip chart recording showing wind direction and speed at the 61-m level on the tower.

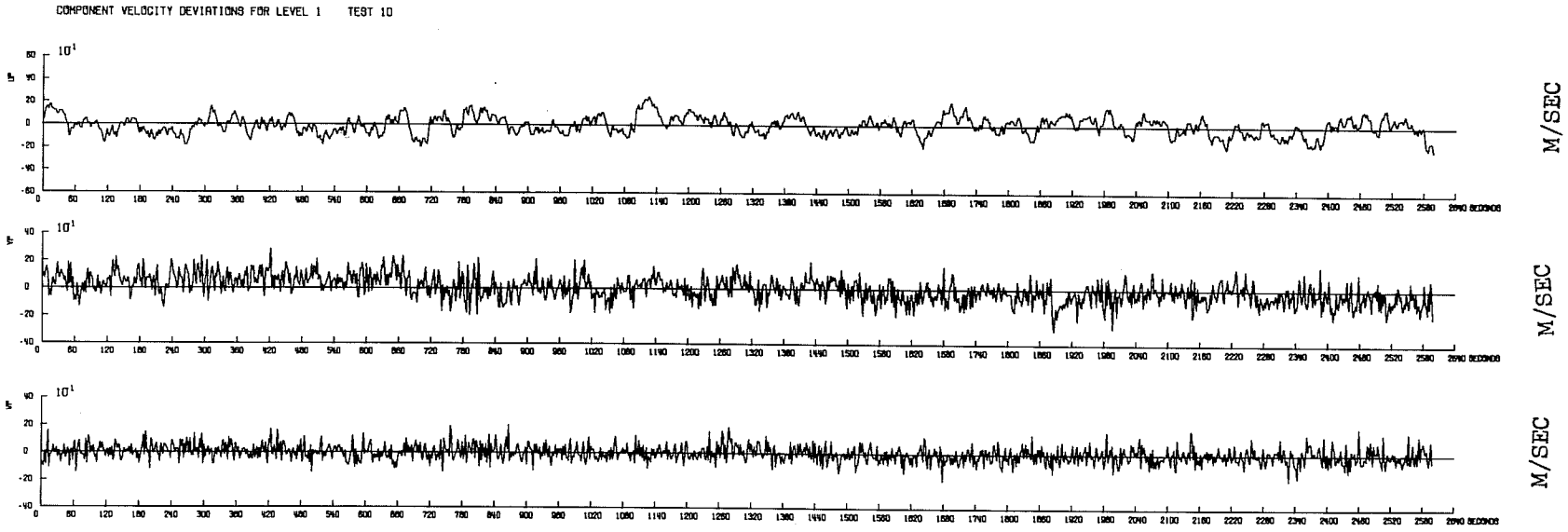

Figure 22. Velocity components, u', v', and w', for the 4-m level in the upper, middle, and lower diagrams. The units on the vertical axis are 10^{-1} m/sec^{-1}.

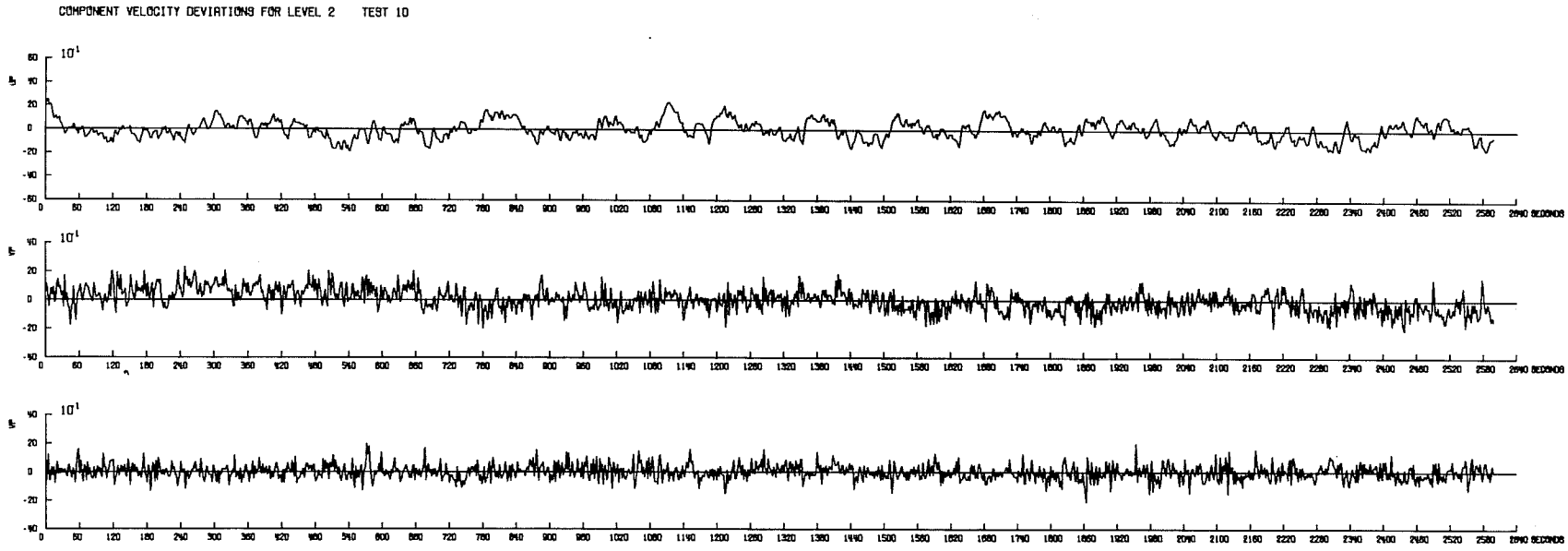

Figure 23. Velocity components, u', v', and w', for the 16-m level, in the upper, middle, and lower diagrams. The units on the vertical axis are 10^{-1} m/sec^{-1}.

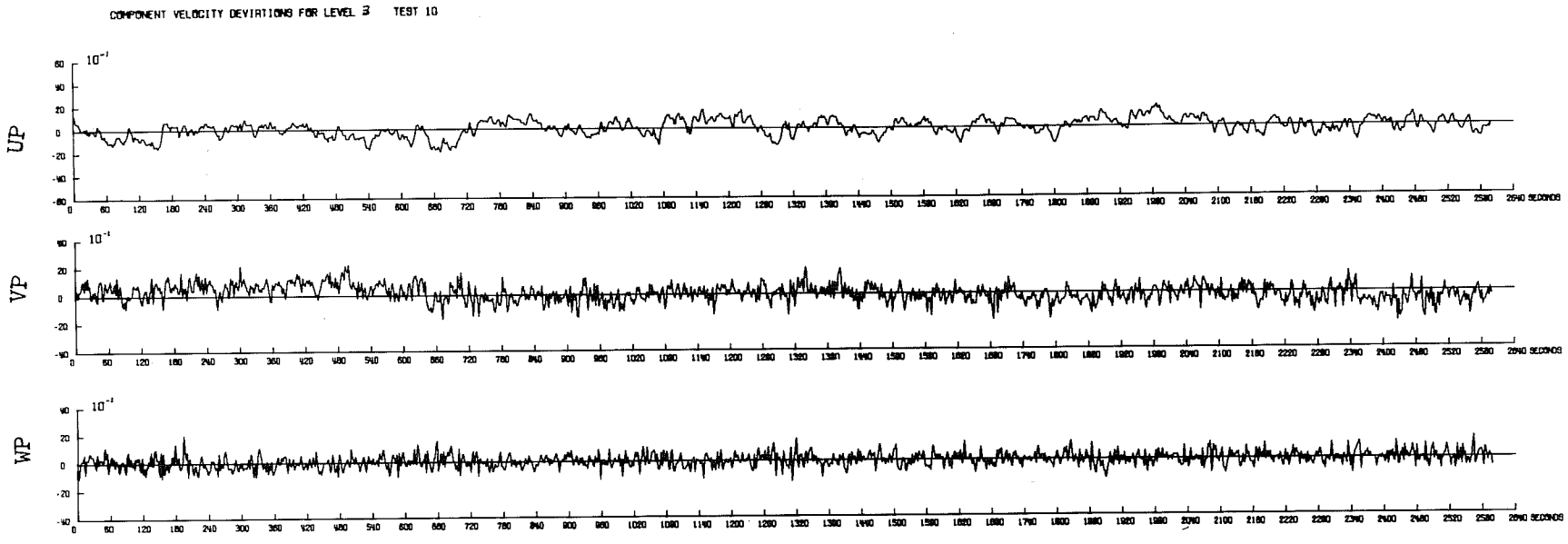

Figure 24. Velocity components, u', v', and w', for the 61-m level, in the upper, middle, and lower diagrams. The units on the vertical axis are 10^{-1} m/sec^{-1}.

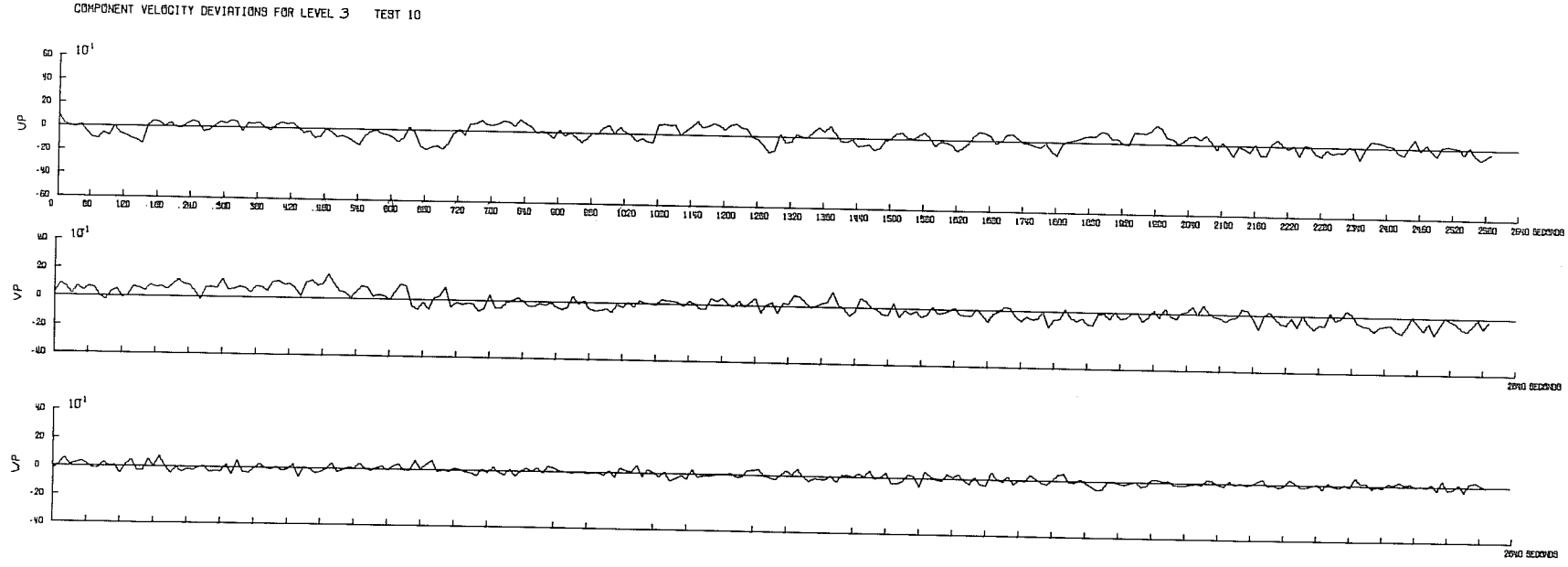

Figure 25. Velocity components, u', v', and w', for the 61-m level, with five-point running average, in the upper, middle, and lower diagrams. The units on the vertical axis are 10^{-1} m/sec^{-1}.

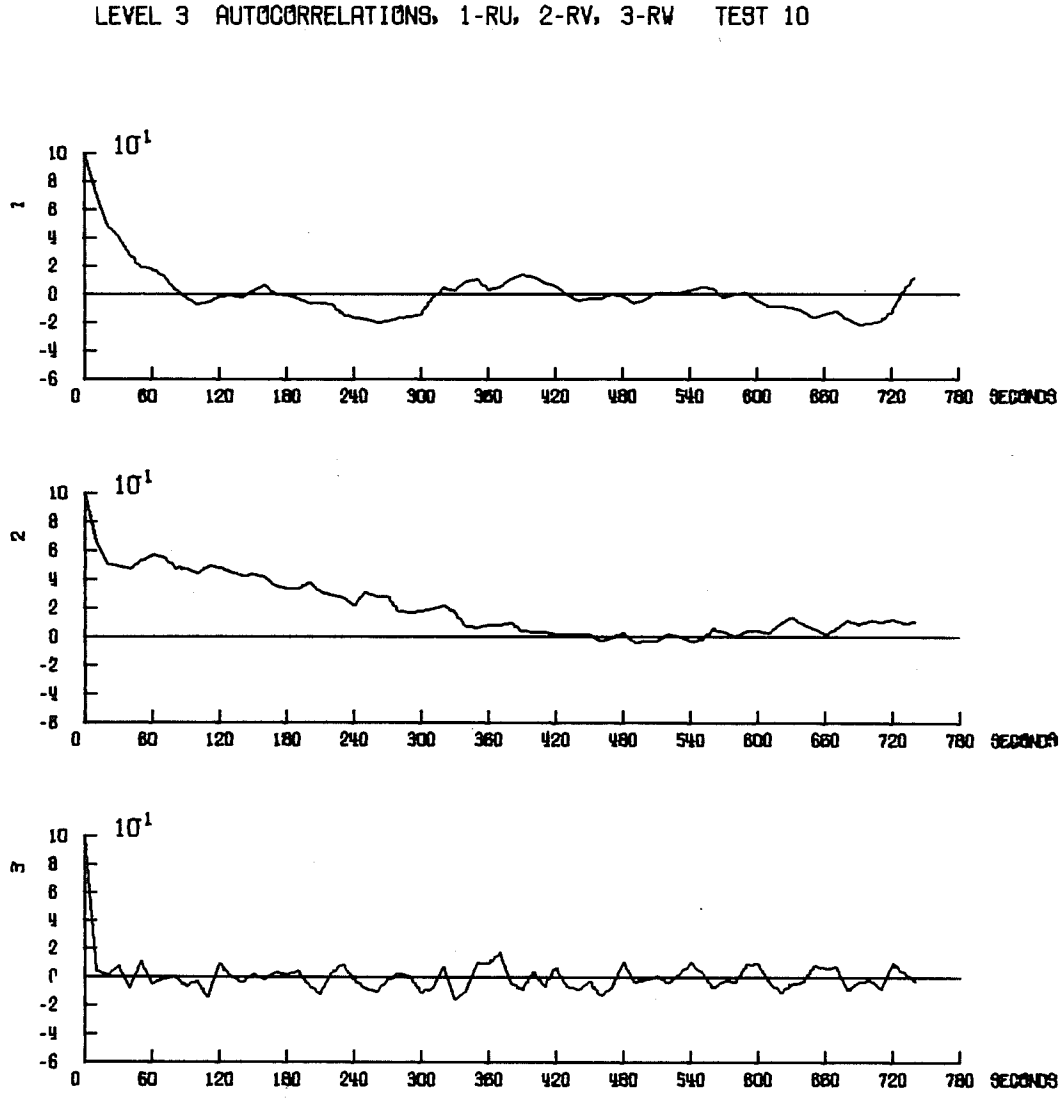

Figure 26. Autocorrelation functions of the velocity components, u, v, and w, are shown in the upper, middle, and lower diagrams.

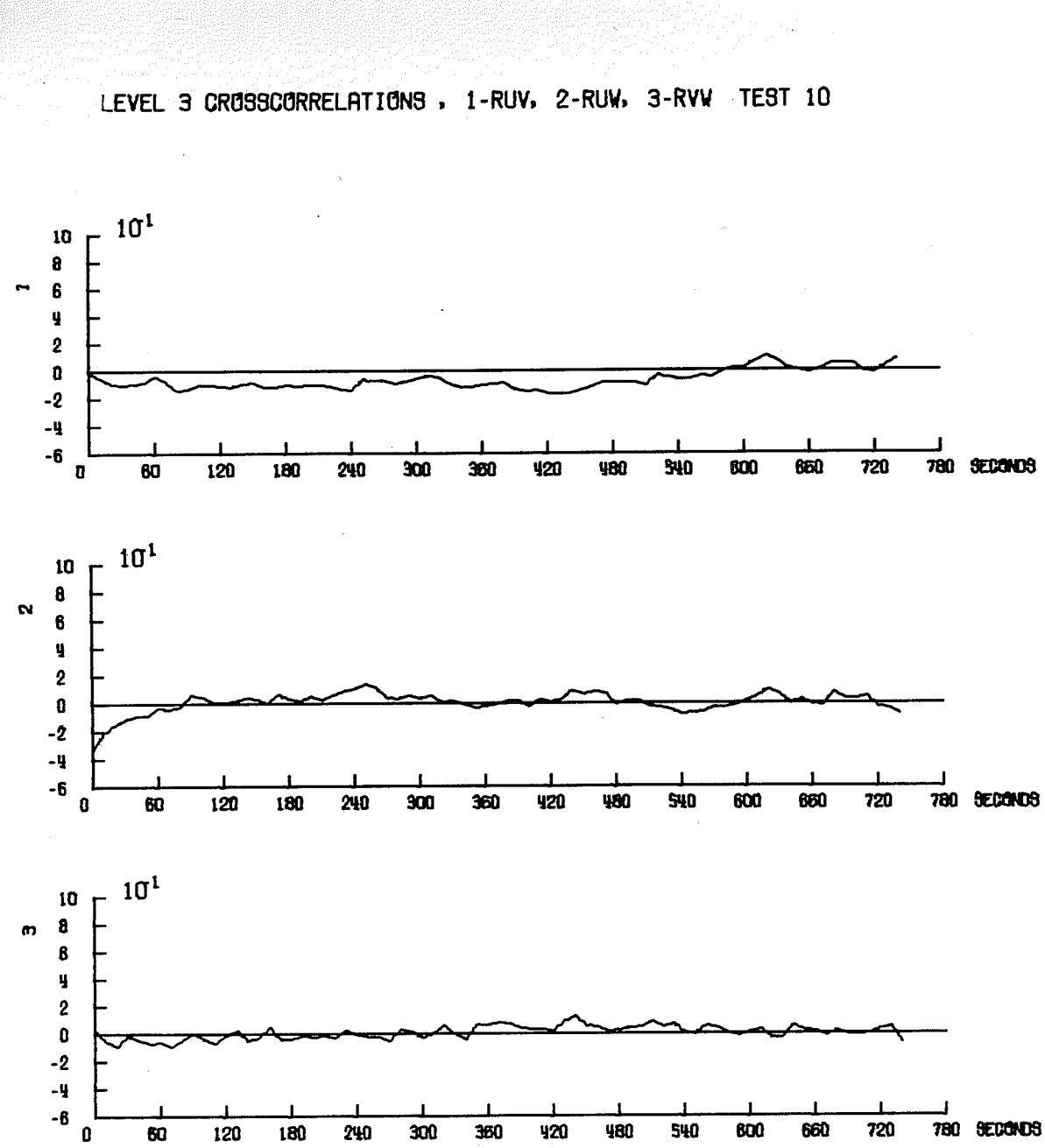

Figure 27. Crosscorrelation functions $R_{uv}(\tau)$, $R_{uw}(\tau)$ and $R_{vw}(\tau)$ are shown in the upper, middle, and lower diagrams.

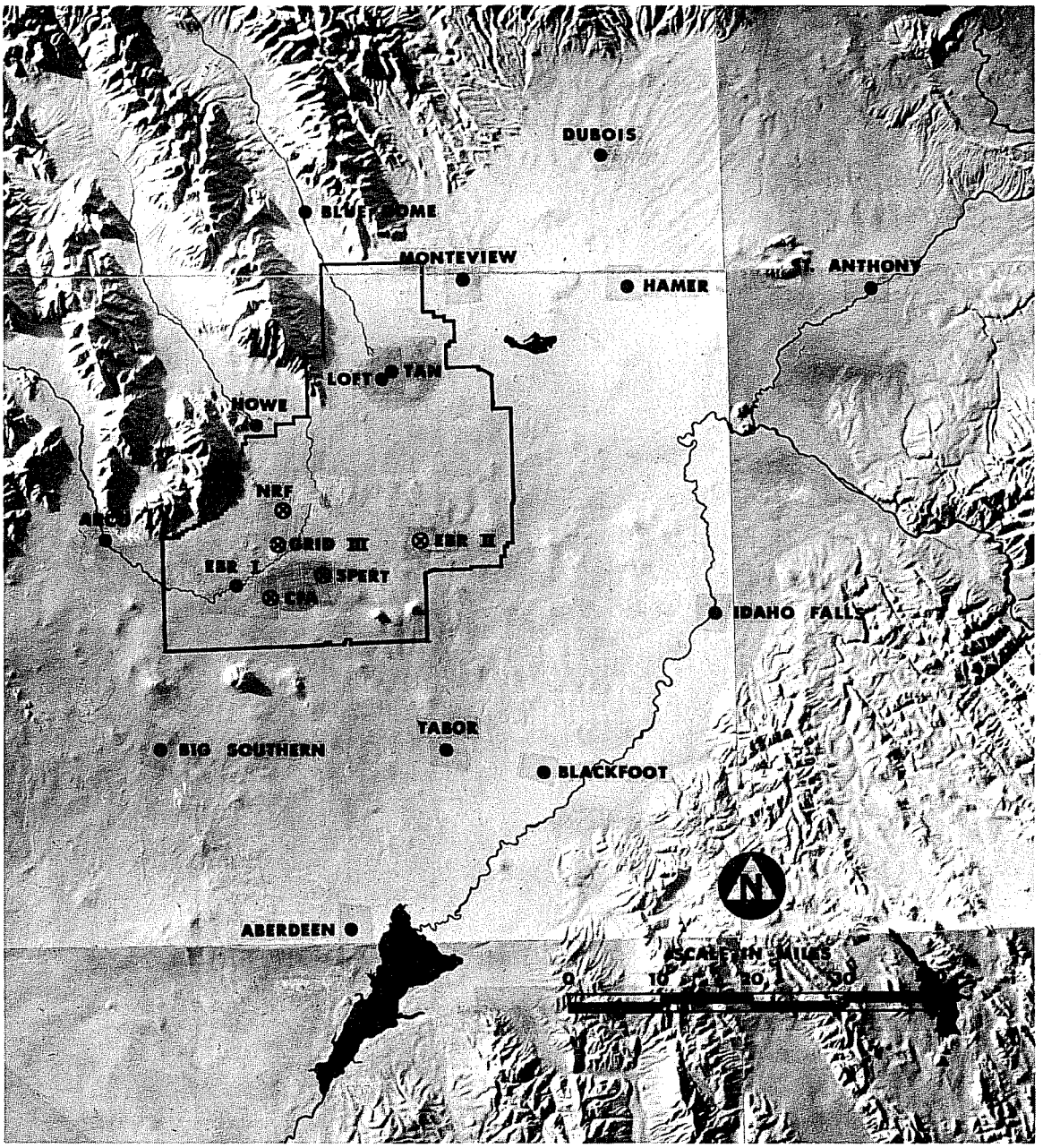

Figure 28. Meso-micrometeorological wind station network.

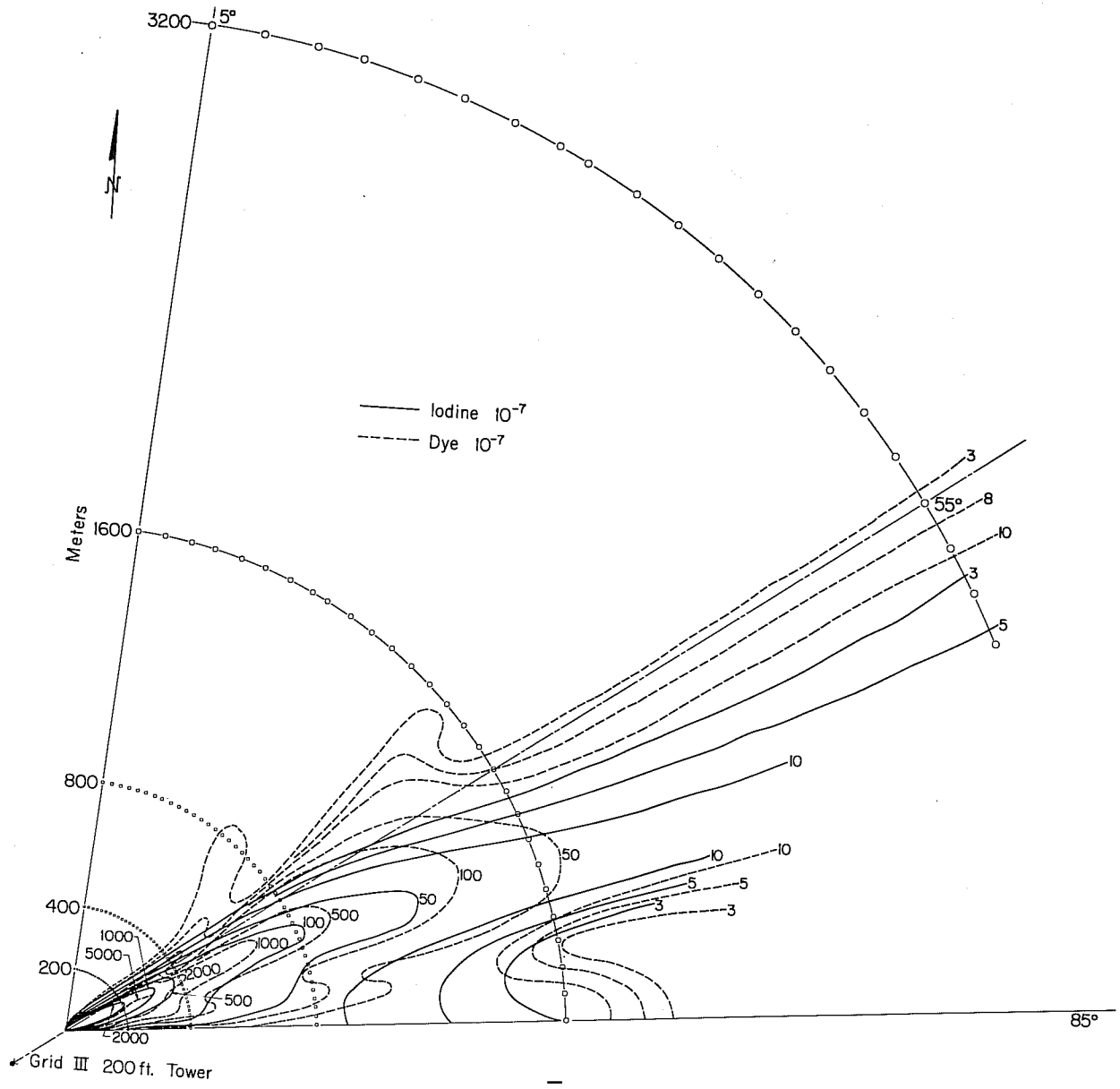

Figure 29. Grid III diffusion site and measured ($\chi\bar{U}/Q$) isopleths of uranine dye (dashed lines) and elemental radioiodine (solid lines).

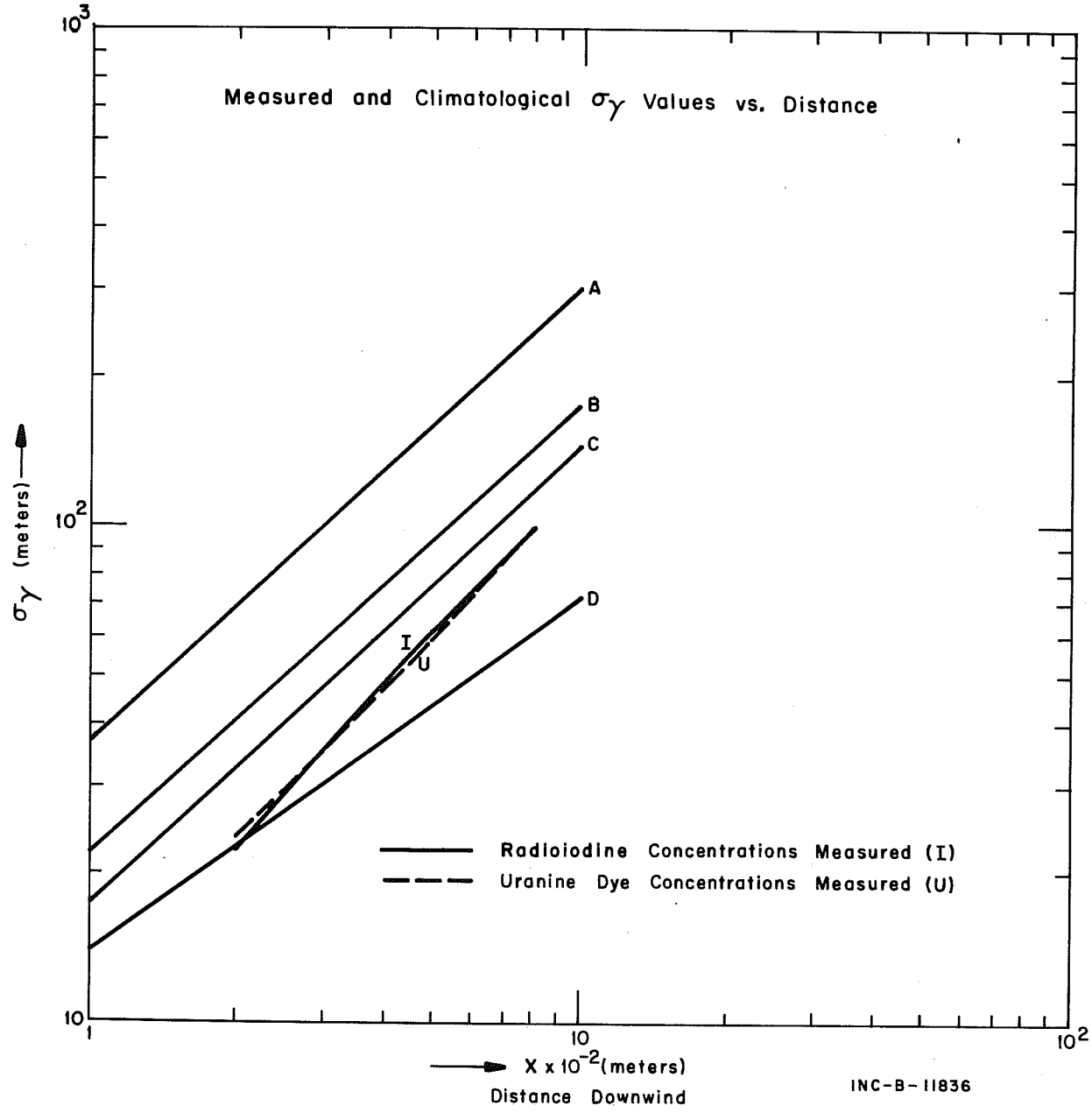

Figure 30. Measured and climatological values of σ_y versus distance.

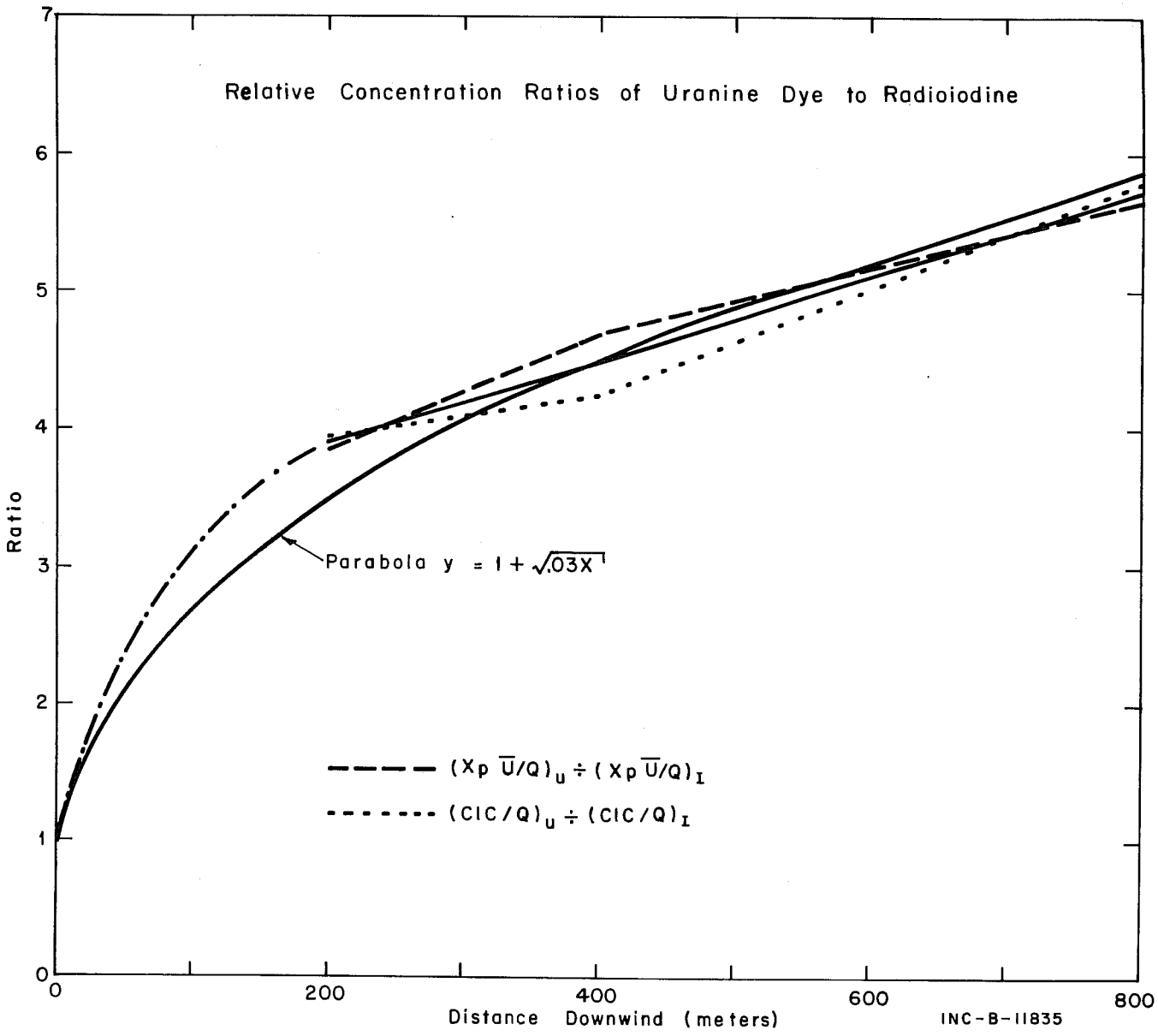

Figure 31. Relative concentration ratios of uranine dye to radioiodine versus distance. The straight solid line is the mean of the dashed and dotted curves, and the dash-dot extension of the mean line indicates the general trend that must occur towards the source.

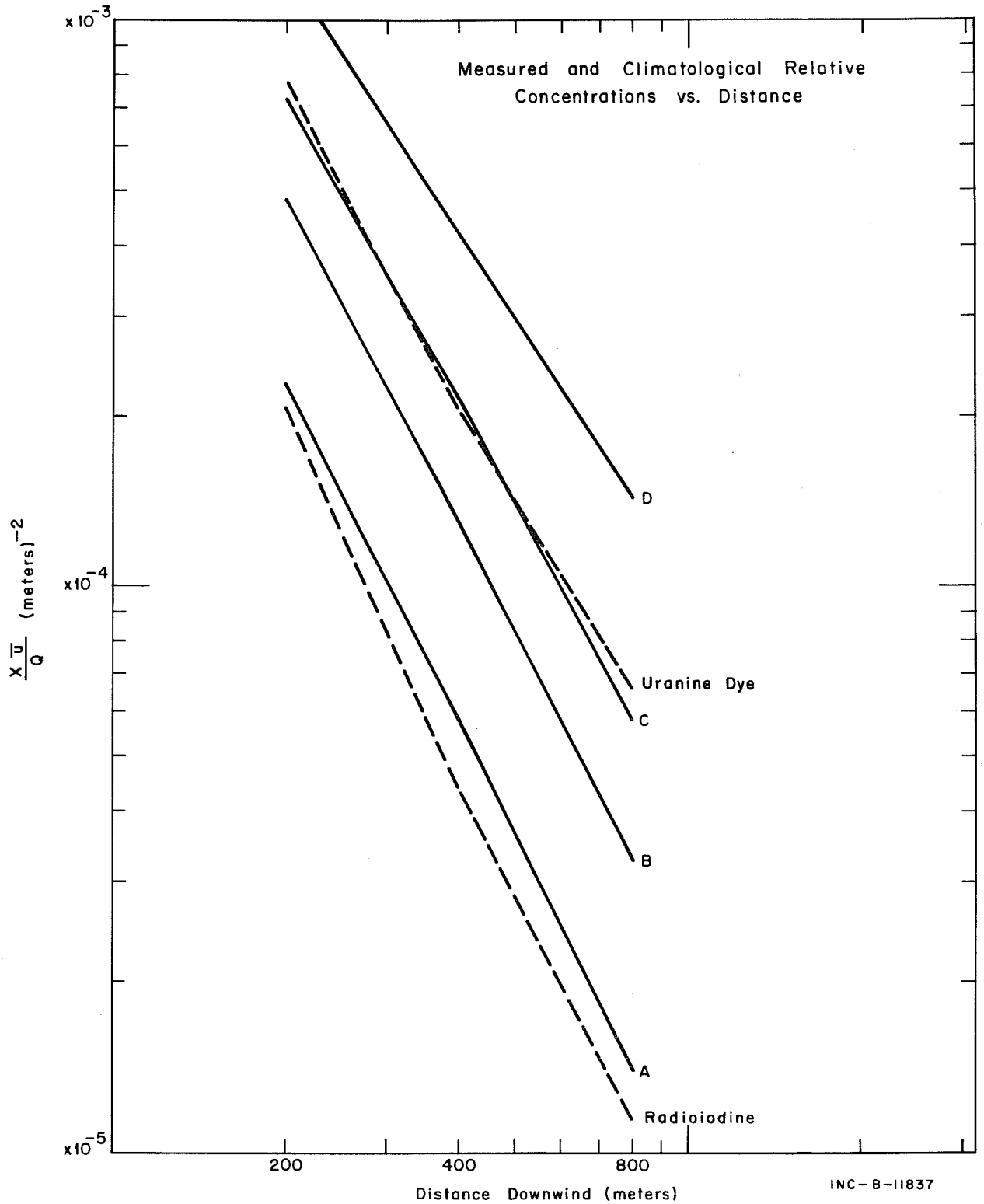

Figure 32. Measured (dashed lines) and climatological (solid lines) peak values of $\chi\bar{u}/Q$ versus distance.

GPO 843-654